https://doi.org/10.5194/acp-2020-1271
Preprint. Discussion started: 29 December 2020

Atmospheric Chemistry and Physics Discussions

UTLS wildfire smoke over the North Pole region, Arctic haze, and aerosol-cloud interaction during MOSAiC 2019/20: An introductory

Ronny Engelmann[1], Albert Ansmann[1], Kevin Ohneiser[1], Hannes Griesche[1], Martin Radenz[1], Julian Hofer[1], Dietrich Althausen[1], Sandro Dahlke[2], Marion Maturilli[2], Igor Veselovskii[3], Cristofer Jimenez[1], Robert Wiesen[1], Holger Baars[1], Johannes Bühl[1], Henriette Gebauer[1], Moritz Haarig[1], Patric Seifert[1], Ulla Wandinger[1], and Andreas Macke[1]

[1]Leibniz Institute for Tropospheric Research, Leipzig, Germany
[2]Alfred Wegener Institute, Helmholtz Centre for Polar and Marine Research, Potsdam, Germany
[3]Prokhorov General Physics Institute of the Russian Academy of Sciences, Moscow, Russia

Correspondence: R. Engelmann
(ronny@tropos.de)

Abstract.

An advanced multiwavelength polarization Raman lidar was operated aboard the icebreaker Polarstern during the MOSAiC (Multidisciplinary drifting Observatory for the Study of Arctic Climate) expedition, lasting from September 2019 to October 2020, to contiuously monitor aerosol and cloud layers in the Central Arctic up to 30 km height at latitudes mostly between 85°N and 88.5°N. The lidar was integrated in a complex remote sensing infrastructure aboard Polarstern. Modern aerosol lidar methods and new lidar techniques and concepts to explore aerosol-cloud interaction were applied for the first time in the Central Arctic. The aim of this introductory article is to provide an overview of the observational spectrum of the lidar products for representative measurement cases. The highlight of the lidar measurements was the detection of a 10 km deep wildfire smoke layer over the North Pole area from, on average, 7 km to 17 km height with an aerosol optical thickness (AOT) at 532 nm around 0.1 (in October-November 2019) and 0.05 from December to mid of March 2020. The wildfire smoke was trapped within the extraordinarily strong polar vortex and remained detectable until the beginning of May 2020. Arctic haze was also monitored and characterized in terms of backscatter, extinction, and extinction-to-backscatter ratio at 355 and 532 nm. High lidar ratios from 60-100 sr in lofted mixed haze and smoke plumes are indicative for the presence of strongly light-absorbing fine-mode particles. The AOT at 532 nm was of the order of 0.025 for the tropospheric haze layers. In addition, so-called cloud closure experiments were applied to Arctic mixed-phase cloud and cirrus observations. The good match between cloud condensation nucleus concentration (CCNC) and cloud droplet number concentration (CDNC) and, on the other hand, between ice-nucleating particle concentration (INPC) and ice crystal number concentration (ICNC) indicated a clear influence of aerosol particles on the evolution of the cloud systems. CDNC was mostly between 20 and 100 cm^{-3} in the liquid-water dominated cloud top layer. ICNC was of the order of 0.1-1 L^{-1}. The study of the impact of wildfire smoke particles on cirrus formation revealed that heterogeneous ice formation with smoke particles (organic aerosol particles) as INPs may have prevailed. ICNC values of 10-40 L^{-1} were clearly below ICNC levels that would indicate homogeneous freezing.

https://doi.org/10.5194/acp-2020-1271
Preprint. Discussion started: 29 December 2020

Atmospheric Chemistry and Physics Discussions

1 Introduction

Rapid sea ice loss, unusual Arctic warming, and our incomplete knowledge about the complex processes controlling the Arctic climate motivated the MOSAiC (Multidisciplinary drifting Observatory for the Study of Arctic Climate) (MOSAiC, 2020) expedition, the largest Arctic research initiative in history. On 26 September 2019, the German research icebreaker Polarstern (Polarstern, 2017) left Tromsø in Northern Norway towards the central part of the Arctic and started drifting through the Arctic Ocean trapped in the ice in the beginning of October 2019. The goal of the MOSAiC expedition was to take the closest look ever at the Arctic as the epicenter of global warming and to gain fundamental insights that are key to better understand global climate change. Hundreds of researchers of more than 70 research institutions from 20 countries were involved in this exceptional expedition. The MOSAiC campaign brought a modern research icebreaker close to the North Pole for a full year especially, for the first time, in polar winter. The mission was spearheaded by the Alfred Wegener Institute, Helmholtz Center for Polar and Marine Research (AWI).

In this article, we provide an overview of our lidar-based contribution to MOSAiC and thus our role in the MOSAiC consortium. We continuously operated a state-of-the-art multiwavelength aerosol/cloud Raman lidar (Engelmann et al., 2016) aboard the research vessel (RV) Polarstern side by side with the ARM (Atmospheric Radiation Measurement) mobile facility 1 (AMF-1) (ARM, 2020) and collected tropospheric and stratospheric aerosol and cloud profile data throughout the expedition period from September 2019 to October 2020. Our goal is (a) to provide a seasonally and height-resolved characterization of aerosol and clouds in the North Pole region from the surface up to 30 km height and (b) to explore the impact of aerosol particles on mixed-phase-cloud and cirrus evolution in the free troposphere up to tropopause level. Aerosol-related ice formation is poorly understood. Advances in our understanding of the role of local and long-transported aerosol pollution in ice formation processes is, however, of fundamental importance for an improved modelling of atmospheric and climate processes in the Arctic. Clouds in general sensitively influence the energy and water cycles, their accurate representation in models is thus critical for robust future climate projections.

Our most impressive and unprecedented observation during the entire MOSAiC expedition was the detection of a persistent, 10 km deep aerosol layer of aged wildfire smoke (aged organic aerosol particles). We monitored this smoke layer in the upper troposphere and lower stratosphere (UTLS) regime from about 5-8 km up to 16-19 km height for seven months from the beginning of the lidar observations in October 2019 until the beginning of May 2020. The wildfire smoke layer originated from severe and huge fires in Siberia, Alaska, and western North America in late summer and autumn of 2019. Hundreds of cirrus layers developed in the smoke layer during the winter half year until the strong Polar vortex, the strongest since 40 years (Lawrence et al., 2020) collapsed at the end of April 2020 and the smoke layer slowly dissolved. The MOSAiC lidar observations (together with the radar observations of the ARM mobile facility) allow us, for the first time, to investigate the role of smoke in ice formation processes and to contrast these findings with respective ones for the summer half year when anthropogenic haze and mineral dust dominate and influence cirrus formation in the Arctic (Grenier et al., 2009; Jouan et al., 2012, 2014). Furthermore, a record-breaking reduction of the ozone concentration, mainly between 15 and 20 km height was found over the Arctic in the spring of 2020 (DeLand et al., 2020; Wohltmann et al., 2020; Innes et al., 2020; Manney et al.,

https://doi.org/10.5194/acp-2020-1271
Preprint. Discussion started: 29 December 2020


Atmospheric Chemistry and Physics Discussions

2020). A unique opportunity is thus given to explore to what extent the wildfire smoke particles, providing a significantly enhanced number of sites for heterogeneous chemical processes (chlorine and bromine activation), contributed to the strong ozone depletion.

The article is organized as follows. After a brief description of the instrumentation and lidar products in Sect. 2, key observations are highlighted in four subsections in Sect. 3. An overview of the smoke situation during the MOSAiC winter half year is given in Sect. 3.1. In Sect. 3.2, we present two cases of Artic haze observations performed in February and March 2020. It is noteworthy to mention that Willis et al. (2019) recently pointed out that the majority of our current knowledge about Arctic aerosol (including their impact on cloud evolution) comes from ground-based in situ monitoring stations. However, with the increasing number of aircraft observations (see the review of Abbatt et al., 2019) and advanced satellite remote sensing, especially after the launch of the spaceborne CALIPSO (Cloud-Aerosol Lidar and Infrared Pathfinder Satellite Observation) lidar (Di Pierro et al., 2013; Di Biagio et al., 2018; Devasthale et al., 2011) it became clear that this view on Artic aerosol conditions is only valid for the lowest several hundreds of meters of the Arctic atmosphere, and only holds for the summer season. The presented observations corroborate that the Arctic free troposphere is significantly polluted during the late winter and early spring months.

In Sect. 3.3 and 3.4 we move on to aerosol-cloud interaction studies. We start with a case of a shallow mixed-phase cloud consisting of a liquid-water layer on top of the ice virga zone. We present a new lidar technique, the so-called dual field-of-view (FOV) polarization lidar technique (Jimenez et al., 2020a, b) that allows us to retrieve the microphysical properties of the liquid-water layer including the cloud droplet number concentration (CDNC) and to combine these observations with lidar-derived estimates of cloud condensation nucleus concentrations (CCNC) around and below the liquid-water cloud layer. Furthermore, we compare the lidar-based estimates of the ice-nucleating particle concentration (INPC) with the ice crystal number concentration (ICNC) derived from combined lidar radar observations (Bühl et al., 2019). Recently introduced new remote sensing analysis concepts (closure studies) (Ansmann et al., 2019) are applied for the first time to Arctic clouds. In Sect. 3.4, the impact of the wildfire smoke on cirrus evolution is illuminated, which can be regarded as a pilot study to explore to what extend wildfire smoke can influence or even control cirrus formation. Organic aerosol particles are ubiquitous in the atmosphere around the world and there is an urgent need to investigate their potential to serve as efficient ice-nucleating particles. MOSAiC provides unique observations to make substantial progress in this research field. The importance and relevance of such smoke-cirrus-interaction studies significantly increased during the last 3-4 years with the increasing number of major wildfire events in both, the northern and southern hemisphere (Baars et al., 2019; Ohneiser et al., 2020), which in turn is probably a result of increased biomass burning in response to a changing climate. Sect. 4 finally provides some concluding remarks.

2 Polarstern cruise, lidar setup, and observational products

Figure 1 shows the track of the drifting RV Polarstern from October 2019 to May 2020. Each of the eight red circles along the Polarstern track indicates the beginning of a new month. The highest northern latitude with 88.6°N was reached around

https://doi.org/10.5194/acp-2020-1271
Preprint. Discussion started: 29 December 2020

Atmospheric Chemistry and Physics Discussions

20 February 2020. The Polarstern was at latitudes ≥85°N from the beginning of October 2019 to the beginning of April 2020. A photograph of the Polarstern in the ice and snow-covered Arctic Ocean is shown in the left panel of Fig. 2 together with a photograph of the main ship-based MOSAiC atmospheric measurement platforms aboard Polarstern (right panel in Fig. 2). Six containers for in situ aerosol monitoring and for active remote sensing of aerosols and clouds with lidars and radars were deployed on the front deck of the research vessel. The ARM (Atmospheric Radiation Measurement) mobile facility AMF-1 on the right side consists of three portable shelters containing a baseline suite of instruments, communication, and data systems.

The OCEANET container of the Leibniz Institute for Tropospheric Research (TROPOS), routinely operated aboard Polarstern since 2009 (Kanitz et al., 2011, 2013; Bohlmann et al., 2018; Yin et al., 2019; Baars et al., 2020) is the third one on the left side of the container spots. Besides continuous observations with our multiwavelength Raman lidar (installed inside the air-conditioned container with specially designed roof window for optimum laser-beam transmittance and sampling of backscattered photons), two microwave radiometers for water vapor and cloud liquid-water measurements, two photometers for aerosol optical thickness (AOT) observations and a two-dimensional disdrometer were operated for ice crystal morphological studies. The TROPOS equipment was already aboard Polarstern two years ago and involved in the Arctic field campaign PASCAL (*P*hysical feedbacks of *A*rctic boundary layer, *S*ea ice, *C*loud and *A*eroso*L*) (Wendisch et al., 2019; Griesche et al., 2020a, b).

2.1 Lidar instrument and operational details

Two advanced lidar instruments, the multiwavelength Raman lidar Polly (*PO*ortab*Le* *L*idar s*Y*stem) (Engelmann et al., 2016) and a High Spectral Resolution Lidar (HSRL) (Eloranta, 2005) were operated aboard the drifting RV Polarstern during the MOSAiC expedition. These two lidars are complementary regarding their capabilities. While the multiwavelength Raman lidar delivered detailed spectrally resolved optical properties of the aerosol in the Arctic and retrieval products regarding microphysical and cloud-relevant aerosol properties from October to March, i.e., during nighttime conditions, the single-wavelength HSRL is of advantage during the summer half year (when Raman lidar observations are of limited use) and allows us to measure profiles of the climate-relevant particle extinction coefficient at 532 nm wavelength even during sunlight conditions. Both lidar systems are polarization lidars and thus permit detailed monitoring of cloud phase and thus of liquid-water, mixed-phase and ice clouds and morphological features (sphericity) of aerosol particles.

The MOSAiC expedition provided for the first time the unique opportunity to perform lidar observations north of 85°N over the entire winter half year 2019-2020. This part of the Central Arctic is not covered by any other lidar measurement, neither by observations with the spaceborne CALIPSO lidar (only up to 81.8°N) nor by measurements of the ground-based Arctic lidar network (Nott and Duck, 2011). Thus, we add a new data set to the global aerosol data base. Di Biagio et al. (2018) were the first to run lidars (mounted on an ensemble of autonomous drifting buoys) in the Central Arctic, even north of 82°N, to perform year-around aerosol profiling, including the winter half year of 2015-2016. These measurements together with respective CALIPSO lidar observations are used in our contrasting analysis regarding the aerosol conditions during the MOSAiC year 2019-2020 and the year 2015-2016 characterized by unperturbed aerosol conditions.

https://doi.org/10.5194/acp-2020-1271
Preprint. Discussion started: 29 December 2020

Atmospheric Chemistry and Physics Discussions

The setup and basic technical details of the Polly instrument are given in Engelmann et al. (2016), Hofer et al. (2017), and Jimenez et al. (2020b). Polly belongs to the lidar network PollyNET (Baars et al., 2016) which is part of the European Aerosol Research Lidar Network (EARLINET) (Pappalardo et al., 2014) organized within the Aerosols, Clouds and Trace gases Research InfraStructure (ACTRIS) project (ACTRIS, 2020). The lidar transmits linearly polarized laser pulses at 355, 532, and 1064 nm with a pulse repetition rate of 20 Hz. All laser beams are pointing to an off-zenith angle of 5° to avoid a bias in the observations of the optical properties of mixed-phase and cirrus clouds caused by strong specular reflection by falling and then frequently horizontally aligned ice crystals (Noel and Sassen, 2005; Noel and Chepfer, 2010; Avery et al., 2020).

The receiver unit consists of a near-range receiver part, optimized to provide aerosol and cloud optical properties from 120 m above the grounds to several kilometers height, and a far-range receiver part which permits accurate aerosol and cloud profiling from about 800 m to 30-40 km height. Thirteen receiver channels are available to collect the following lidar return signals: elastically backscattered photons at the three laser wavelengths, the cross-polarized signal components at 355 and 532 nm (orthogonal to the polarization plane of the linearly polarized laser pulses at two different field of views, FOV), the vibrational Raman signals of nitrogen at 387 and 607 nm, and of water vapor at 407 nm. All signals are measured with photon-counting photomultipliers and stored with 30 seconds of resolution.

The recently introduced and implemented dual-FOV polarization lidar option (Jimenez et al., 2020a, b) permits the measurement of the cross and total (cross and co-polarized) signal components at 532 nm at two different FOVs. This technique enables us to determine multiple scattering by droplets in liquid-water dominated cloud layers and to determine from this multiple scattering information cloud microphysical properties (e.g. effective droplet size and cloud extinction coefficient) (Jimenez et al., 2020a). The method is based on depolarization ratio (ratio of cross-to-co-polarized backscatter coefficient) observations at the two FOVs.

The Polly instrument is designed for automated continuous profiling of aerosols and clouds and thus was running around the clock. Well-defined breaks were necessary to exchange laser flash lamps, to run different calibration procedures, and to check the full setup and to perform an overall alignment of the Polly instrument. Five TROPOS lidar scientists took care of the OCEANET instrumentation over the one-year MOSAiC expedition period.

As an important contribution to MOSAiC, radiosondes were routinely launched every 6 hours throughout the entire MOSAiC period. In our lidar data analysis and discussion of the results, we use the preliminary radiosonde products that were directly available during the expedition.

2.2 Lidar products

The measurement and retrieval products obtained from the multiwavelength dual-FOV polarization and Raman lidar Polly are listed in Table 1. The basic data analysis procedure to obtain aerosol and cloud optical properties (backscatter and extinction coefficients, extinction-to-backscatter or lidar ratio, and linear depolarization ratio profiles) at two or three wavelengths are described by Baars et al. (2012), Baars et al. (2016), Hofer et al. (2017), Haarig et al. (2018), and Ohneiser et al. (2020). The backscatter coefficients can be obtained with the highest vertical resolution of 7.5 m and are preferably used to characteirze the geometrical properties of detected aerosol layers. The particle extinction coefficient is the most important parameter in

https://doi.org/10.5194/acp-2020-1271
Preprint. Discussion started: 29 December 2020

Atmospheric Chemistry and Physics Discussions

radiative transfer studies. The lidar ratio of aerosol particles is an important quantity in aerosol typing efforts because it is sensitive to the ratio of absorption to scattering by the particles (Müller et al., 2007) and is low for marine particles (around 15-20 sr) and can be very high for light-absorbing particles (100-120 sr) (Ohneiser et al., 2020). The linear depolarization ratio is defined as the cross-polarized-to-co-polarized backscatter ratio and allows us to sensitively distinguish spherical particles showing particle linear depolarization ratios (PLDR) close to zero from non-spherical aerosol particles showing PLDR values of typically 0.1-0.3. In the case of clouds, liquid-droplet layers show PLDR≈ 0 at layer base where light depolarizing multiple scattering is low, and PLDR of 0.4-0.6 in, e.g., cirrus layers. "Co" and "cross" denote the planes of polarization parallel and orthogonal to the plane of linear polarization of the transmitted laser pulses, respectively.

The retrieval of aerosol microphysical properties such as particle volume, mass, and surface area concentration and estimates of cloud-relevant properties (aerosol-type-dependent cloud condensation nuclei, CCN, and ice-nucleating particles, INPs) is performed by means of the POLIPHON (Polarization Lidar Photometer Networking) approach (Mamouri and Ansmann, 2016, 2017; Ansmann et al., 2019, 2020). Hofer et al. (2020) exemplary shows the full set of POLIPHON aerosol products in the cases of an 18-month Polly campaign in Dushanbe, Tajikistan, for central Asian aerosol. Alternatively to the POLIPHON method, we used the multiwavelength lidar inversion technique (Müller et al., 1999, 2014; Veselovskii et al., 2002, 2012) to derive microphysical properties of aerosols including the particle size distribution for detected pronounced aerosol layers. Details of the retrieval of microphysical properties of liquid-water cloud layers can be found in Jimenez et al. (2020a, b). Regarding the determination of height profiles of the water-vapor-to-dry-air mixing ratio from the Raman lidar observations of water vapor and nitrogen vibrational Raman signals we follow the procedure described by Dai et al. (2018). Relative humidity is obtained from the mixing-ratio measurements and temperature profiles measured regularly (four times a day) aboard Polarstern. Quality checks of the continuously obtained water vapor fields is based on comparisons with the relative-humidity profiles obtained with radiosondes.

Radiosonde temperature and pressure profiles are used in the lidar data analysis to correct for Rayleigh backscattering and attenuation effects on the measured lidar signal profiles. Temporal averaging and vertical smoothing of signal profiles were applied to reduce the impact of signal noise. Corrections of the incomplete overlap between laser beam and receiver FOVs in the lidar near-range are needed to extend the observational range to very low heights above the lidar, down to 120 m.

3 Observations

We begin with a few impressions (snapshots) of typical aerosol and cloud scenes observed with our lidar during the winter months. According to Fig. 1, the Polarstern moved very slowly with the pack ice in December, January, and February and was mostly located between 86°N and 88°N. The exceptionally strong polar vortex of 2019-2020 was well established to that time. Figure 3 shows a 10-day measurement sequence (2-12 Dec 2019). Complex features of aerosol layering, cirrus evolution (Fig. 3a-d), and mixed-phase cloud life cycles (Fig. 3e-f) were found. Clear, fog, and cloud free periods occurred frequently as well and provided excellent conditions for a detailed characterization of Arctic haze and wildfire smoke. These observations in Fig. 3c-h will be discussed in detail in Sect. 3.1, 3.4, and 3.5.

https://doi.org/10.5194/acp-2020-1271
Preprint. Discussion started: 29 December 2020


Atmospheric Chemistry and Physics Discussions

The measured linear depolarization ratio in the right panels of Fig. 3 allows us to precisely distinguish cirrus from layered mixed-phase clouds as explained above. Ice crystals cause large depolarization ratios (green to red colors in Fig. 3b, d, f), and, in contrast, liquid-water layers produce rather low depolarization ratios around zero in Fig. 3f. The increase of the depolarization values with increasing penetration of the laser beam into the water cloud layer is caused by multiple scattering by the cloud droplets. This aspect is explained in more detail in Sect. 3.3. The depolarization ratio of aerosol particles was found to be generally small (Fig. 3h) in the free troposphere and stratosphere which indicates spherical haze and smoke particles.

3.1 Wildfire smoke layer in the UTLS regime

According to Stohl (2006) the aerosol conditions in the Arctic troposphere up to UTLS heights are controlled by aerosol long-range transport. Stohl (2006) identified three major pathways. The winter transport of aerosols (regime 1), mainly from Asian and European sources towards the high Arctic occurs at low heights and long-transported aerosols may reach heights up to the middle troposphere (5-7 km height). In summer, warm, moist and polluted air massed mainly originating from North America and Asia are forced to ascend during long range transport and thus reach the colder Arctic at heights in the middle and upper troposphere. Two mechanisms are then active. Either, uplift of air masses occurs at the Arctic front after low-level northward transport (regime 2) or the mid-latitude air masses are lifted over the source regions (such as wild fire smoke) followed by high-altitude transport in northerly directions (regime 3). All this is described by Stohl (2006), Law and Stohl (2007), Law et al. (2014), and Bozem et al. (2019). A fourth mechanism (quite similar to the third one) became relevant during the last few years and is characterized by a rather fast ascent of wildfire smoke up to the tropopause and occasionally into the lower stratosphere via pyro-cumulonimbus (pyro-Cb) convection over areas with intense and long-lasting fires (Fromm and Servranckx, 2003; Fromm et al., 2010; Peterson et al., 2018; Khaykin et al., 2018; Ansmann et al., 2018; Hu et al., 2019; Zuev et al., 2019), immediately followed by further ascent due to self-lifting processes caused by absorption of solar radiation and heating of the smoke-containing air layers (Boers et al., 2010; de Laat et al., 2012; Torres et al., 2020; Ohneiser et al., 2020; Kablick et al., 2020; Khaykin et al., 2020). The light-absorption-related lifting occurs during the spread of the smoke over the respective hemisphere and continues as long as the smoke layers are optically dense enough (aerosol optical thickness AOT$>$1-2 at 500 nm) with the consequence that the smoke reaches, e.g., the Central Arctic at heights up to 5-10 km above the tropopause. Law and Stohl (2007) already mentioned the potentially strong impact of pyro-Cb activity on the vertical smoke distribution, but to that time this transport pathway was of minor importance. This fourth mechanism is responsible for the occurrence of ULTS wildfire smoke over the North Pole region in the MOSAiC winter half year. Fromm et al. (2008), Yu et al. (2019), Bourassa et al. (2019), Baars et al. (2019), and Jumelet et al. (2020) documented that a polward transport of pyro-Cb-related fire smoke is possible within few weeks.

Figure 4 presents the optical properties of the smoke layer as measured on 11 December 2019 (Fig. 3g and h). The smoke layer extended from 8 to more than 18 km height. The internal vertical structures were rather smooth and indicate an aged smoke layer. A clear indication and striking feature for the dominance of smoke particles is the observed spectral dependence of the extinction-to-backscatter ratio (Fig. 4d). The 532 nm lidar ratio is much larger than the 355 nm lidar ratio. This is an

https://doi.org/10.5194/acp-2020-1271
Preprint. Discussion started: 29 December 2020


Atmospheric Chemistry and Physics Discussions

unambiguous indication for the presence of aged biomass burning smoke. No other aerosol type (or cloud type) produces an inverse spectral behavior in terms of the particle lidar ratio (Müller et al., 2005; Haarig et al., 2018; Ohneiser et al., 2020).

The unusual spectral behavior of the lidar ratio is related to the strong wavelength dependence of the backscatter coefficient and the weak spectral dependence of the extinction coefficient (Fig. 4a and c). These specific optical properties are linked to the narrow size distribution of absorbing smoke particles which form a well-defined accumulation mode as shown in Fig. 5. The size distributions of the smoke particles were obtained from the Polly observation by applying the lidar inversion method to the layer-mean backscatter and extinction information (Veselovskii et al., 2012). In agreement with many in-situ observations of long-transported aged smoke (Fiebig et al., 2003; Petzold et al., 2007; Dahlkötter et al., 2014), an accumulation mode with a comparably large mode radius of 250-300 nm (for the volume size distribution) was found in October and November 2019. A distinct coarse mode was absent.

As already mentioned, the particle depolarization ratios at 532 nm (around 1%) and at 355 nm (1-2%) were very low and indicated spherical particles (Fig. 4b). Assuming a core-shell structure of the smoke particles, slight deviations from the spherical shape (probably caused by an irregular black-carbon-containing core structure) can lead to depolarization ratios of up to 0.2 at 532 nm (Haarig et al., 2018; Gialitaki et al., 2020; Ohneiser et al., 2020). With increasing age the core structure obviously collapses, gets compact, and the particles become more and more spherical with time (Baars et al., 2019).

An overview of the smoke conditions during the MOSAiC winter half year (October to April) is presented in Figure 6. Usually, one observation per day is considered. Gaps in the observations are caused by long-lasting low level fog and low-cloud events. The maximum smoke concentration was found around or just below the tropopause (Fig. 6a). In the computation of the tropopause height from the radiosonde data we used a refined version of the World Meteorological Organization approach (WMO, 1992; Klehr, 2012). Most of the time, the smoke layer was observed between 7 and 17 km height. A trend of downward motion is not visible. The maximum extinction coefficients (532 nm) around the tropopause slowly decreased with time from values >10 Mm^{-1} in October and November to <5 Mm^{-1} in April 2020 (Fig. 6a).

In terms of the aerosol optical thickness (AOT) for 532 nm, shown in Fig. 6b, the perturbation decreased from 0.09–0.12 in October and November to values of 0.03-0.06 in December to February, and dropped to 0.01 in April 2020. Almost constant AOT conditions were observed from the end of November to the beginning of March. During this time period the extraordinarily strong polar vortex was well established and obviously prohibited any mixing with less-polluted air from outside the central Arctic. Downward mixing and transport into the lower troposphere had no impact on the UTLS AOT as well. The vortex collapsed around 20 April (Lawrence et al., 2020).

The layer-mean 532 nm smoke extinction coefficients in Fig. 6c (obtained from the ratio of AOT divided by the layer geometrical depth in Fig. 6a) were on the order of 10 Mm^{-1} in October, around 4-5 Mm^{-1} during the main winter months and mostly $\leq$3 Mm^{-1} at the end of the life time of the smoke layer. From the measured layer-mean extinction coefficients mass concentrations of the smoke particles were derived (Ansmann et al., 2020) and ranged from 0.5–1.8 μg m^{-3} during the autumn and winter months. Note that AOT values for a clean stratosphere are around 0.001-0.002 (Sakai et al., 2016; Baars et al., 2019), minimum extinction coefficients of the order of 0.1-0.2 Mm^{-1}, and minimum stratospheric mass concentrations are close to 0.01-0.02 μg m^{-3}.

https://doi.org/10.5194/acp-2020-1271
Preprint. Discussion started: 29 December 2020

Atmospheric Chemistry and Physics Discussions

It is noteworthy to mention that the CALIPSO data base (CALIPSO, 2020a, b) does not contain clear hints on the Arctic UTLS aerosol layer observed continuously over the RV Polarstern. According to HYSPLIT (Hybrid Single-Particle Lagrangian Integrated Trajectory-Model) backward trajectories (HYSPLIT, 2020), satellite remote sensing (Kloss et al., 2020), and ground-based Raman lidar observations of the Alfred Wegener Institute at Spitsbergen (Ohneiser et al., 2021), the aerosol layer covered large parts of the Arctic and thus should have been detectable along the CALIPSO flight track (south of 81.8°N). One of the reasons is probably that the CALIPSO data analysis scheme searches for aerosol features (layers) producing a clearly detectable increase and decrease in backscatter intensity at the layer boundaries. But this smoke layer had no clear boundaries, at least no clear upper boundary (see Figure 4a). Furthermore, the maximum backscatter values ($<$0.2 Mm^{-1} sr^{-1}) were too low to be clearly detected by the CALIPSO lidar. Di Biagio et al. (2018) discuss CALIPSO lidar detection limits in the case of Arctic aerosol observations and corroborate our hypothesis.

Probably as a consequence of the missing aerosol information in the CALIPSO data base, the potential impact of the Arctic wildfire smoke on the strong ozone reduction (in the height range from 12-22 km height) in early spring 2020 remained completely unconsidered in the discussion of the reasons for the observed record-breaking ozone depletion (DeLand et al., 2020; Wohltmann et al., 2020; Innes et al., 2020; Manney et al., 2020). Only polar stratospheric clouds (PSC) were taken into account in the ozone-hole analysis. However, in contrast to PSCs, which developed from December to April (according to CALIPSO observations) (Ohneiser et al., 2021) the smoke layer was continuously present and probably homogeneously distributed over large areas of the Arctic. The significantly enhanced particle surface area concentration may have triggered early chlorine and bromine activation, already in November 2019. As Innes et al. (2020) stated, the ozone depletion started earlier in the winter of 2019-2020 than in other years with strong ozone reduction. And the largest ozone depletion was observed at comparably low heights of 15-20 km.

A PSC observation is shown in Fig. 7. Note that we corrected our stratospheric smoke observations in Fig. 6 for PSC effects. According to the PSC classification scheme (Achtert and Tesche, 2014), we observed a type Ib PSCs. This type is made up of supercooled liquid ternary solutions that consist of H_2SO_4, HNO_3, and H_2O. In contrast to type Ia and II PSC particles (crystals) the liquid droplets of PSC type Ib only slightly depolarize incoming laser light. The temperature at PSC base height showed values of -78°C and at the backscatter maximum the Polarstern radiosonde measured a temperature of -86°C. We observed a much lower number of PSCs over the North Pole region (86° to 88.6°N) than the CALIPSO lidar (60° to 81.8°N) where most of the ozone depletion occurred. Further discussion of our PSC observations and on the link between smoke, PSCs, and the height range of the largest ozone depletion is given by Ohneiser et al. (2021).

At the end of this section, we need to discuss a potential contribution of volcanic aerosol to the UTLS aerosol pollution. Besides the record-breaking fires at high northern latitudes, a strong eruption of the Raikoke volcano in the Kuril Islands (48.3°N, 153.3°E) occurred on 22 June 2019 and influenced the stratospheric aerosol conditions in the northern hemisphere. Kloss et al. (2020) emphasized this impact and the spread of the volcanic aerosol over all latitudes $>$50°N, especially from August to October 2019. According to Vaughan et al. (2020), the volcanic aerosol layer consisting of sulfuric-acid-containing water droplets (75% H_2SO_4, 25% H_2O) formed above the tropopause with maximum heights reaching 21 km. From the 355 nm Raman lidar observations at Capel Dewi Atmospheric Observatory, United Kingdom (52.4°N, 4.1°W) it can be concluded that

https://doi.org/10.5194/acp-2020-1271
Preprint. Discussion started: 29 December 2020


Atmospheric Chemistry and Physics Discussions

the 532 nm AOT was about 0.03 over UK in August 2019, of the order of 0.01 in December, and of around 0.005 during the first months of 2020, respectively. A similar perturbation must be considered for the Central Arctic (Kloss et al., 2020). However, our observations of the aerosol optical properties suggest only a minor contribution of remaining volcanic aerosol particles on the found UTLS aerosol layer. As presented by Ohneiser et al. (2021), the UTLS particle lidar ratios mainly ranged from 50-70 sr at 355 nm and 70-90 sr at 532 nm during the winter half year of 2019-2020. These values are considerably higher than typical volcanic aerosol lidar ratios observable within several months after the sulfuric acid aerosol formation (Wandinger et al., 1995; Jäger and Deshler, 2003). Mattis et al. (2010) reported lidar ratios of around 40 sr for both wavelengths after a similar volcanic eruption in 2009. A detailed discussion on this topic is given in Ohneiser et al. (2021).

3.2 Arctic haze vertical structures

The original and primary goal of the shipborne MOSAiC lidar measurements was to provide, for the first time, a seasonally and height-resolved characterization of tropospheric aerosols and clouds for the North Pole region. Especially the coverage of the winter half year can be regarded as a valuable new contribution to Arctic aerosol research. Height-resolved lidar observations of Arctic haze, prevailing during the late winter and early spring months, are rare (Di Pierro et al., 2013; Di Biagio et al., 2018). Because of its importance for the climate and environmental conditions in the Arctic, these aged haze aerosols have been intensively studied since more than 50 years (Law et al., 2014; Willis et al., 2018; Abbatt et al., 2019). However, knowledge about the vertical layering structures of Arctic haze is still limited and mostly based on snaphshot-like aircraft observations performed during field campaigns, preferably in spring. As summarized by Willis et al. (2018), long-range transport of cold, polluted air masses from northern Eurasian source regions (mainly north of the Arctic front) prevails in winter and is the reason for the development of Arctic Haze. Mass concentrations are highest in late winter and early spring. Such a low-level aerosol transport is missing in summer.

In Fig. 8, we present two MOSAiC cases observed on 4 February and 4 March 2020 to discuss typical features of Arctic haze. The measurements are representative for many days during the winter months. RV Polarstern was drifting with the ice at latitudes of 87.5°N (4 February) and 88.1°N (4 March). The most striking feature in both figures is that aerosol layers were detected everywhere up to the tropopause, and because of the smoke layer even from 8 to almost 20 km height. There were no regions with a negligible aerosol content. Remnants of PSCs were visible around 13.5–14 km height in Fig. 8a. Temperatures were around -76°C at 13.5 km height and thus sufficiently low to allow formation of type Ia PSC (Achtert and Tesche, 2014; DeLand et al., 2020). Type-Ia PSCs consist of nitric acid trihydrate (NAT) crystals and produce significant depolarization of backscattered laser light.

According to the backward trajectory analysis shown in Fig. 9 (HYSPLIT, 2020), the aerosol pollution in the pronounced aerosol layers around 5 km (4 February, 11 UTC, Fig. 8a) and 4 km height (4 March, 11 UTC, Fig. 8b) originated from central and western European regions (4 February) and from Russia and the Black Sea area (4 March). However, a clear identification of the source region was impossible. The height-resolved trajectory analysis indicated that most of the aeorosol circled around in the Arctic (at latitudes > 70°N) for more than a week before crossing the Polarstern.

https://doi.org/10.5194/acp-2020-1271
Preprint. Discussion started: 29 December 2020


Atmospheric Chemistry and Physics Discussions

In Fig. 10, the optical properties of Arctic haze for the two cases are illustrated. 12-hour (4 February) and 18-hour (4 March) mean height profiles of the basic lidar products (backscatter, extinction, extinction-to-backscatter ratio) are shown. In both cases, we found a near surface layer up to about 2.5 km height and a separated lofted aerosol layer up to 5 and 7 km height. A clear wavelength dependence of the backscatter and extinction coefficients was found on 4 March, as expected for fine-mode dominated particles in the Arctic (Quennehen et al., 2012) consisting of a mixture of anthropogenic haze and fire smoke (Wang et al., 2011). The Ångström exponent for the extinction coefficient was around 1.7 in the lofted layer above 3 km height. The lidar ratios were high with values close to 100 sr in the lofted layer on 4 March. This is indicative of the presence of small, strongly light-absorbing particles (Müller et al., 2007).

Our findings are in agreement with the results previously published and obtained during major field activities such as POLARCAT-IPY (Polar Study using Aircraft, Remote Sensing, Surface Measurements, and Models, of Climate, Chemistry, Aerosols, and Transport, International Polar Year) (Law et al., 2014) as well during ARCTAS (Arctic Research of the Composition of the Troposphere from Aircraft and Satellites) (Wang et al., 2011). Both campaigns took place in the spring of 2008. Arctic haze was mostly found up to 7 km height. The aerosol composition was analyzed in large detail based on aircraft observations.

Wang et al. (2011) summarized and reviewed earlier Arctic observations with their model calculations and found that the ratio of black carbon (BC) to organic aerosol (OA) is high with values of 0.1–0.15 for aerosols advected from Russia, a mixture of anthropogenic haze and domestic, forest, and agricultural fire smoke. OA and sulfate are the dominant components of the fine-mode aerosol. Sulfate is dominant in surface air but OA becomes comparably large in the free troposphere, because sulfate shows little variation with altitude while OA is strongly peaked at 2–6 km. Open fires were found to be the dominant source of OA at all altitudes in the model, but anthropogenic sources are more important for BC and dominate near the surface.

Agricultural fires during spring (Europe, Asia) and flaring of natural gas (Russian oil industry) are important sources for black carbon particles. Eurasian fires mix with anthropogenic haze mainly from Asia during the long-range transport towards the central Arctic, probably beginning in late winter and with peak occurrence in the spring season (Wang et al., 2011). Agricultural and forest fires produce BC/OA ratios of typically <0.1 whereas anthropogenic haze may cause ratios >0.15. It was observed during the POLARCAT-IPY and ACTRAS that the impact of fire aerosol increases with height.

On 4 Februay 2020 (Fig. 10a), the aerosol optical properties were less well defined, the extinction coefficients were almost equal at both wavelengths (355 and 532 nm), and the noisy lidar ratios at 532 nm were larger than at 355 nm in the lofted layer above 3 km height which is typical for aged wildfire smoke as discussed in the foregoing section. The lidar ratios were lower than on 4 March, i.e., less absorbing particles were present. The volume depolarization ratios were rather low in both cases and indicated the dominance of aerosol pollution (spherical particles). The 532 nm AOT was 0.024 (4 February, for the lowest 7 km height) and 0.022 (4 March, for the lowest 5 km), and thus considerably lower than the UTLS smoke AOT of 0.04–0.05.

The values for the extinction coefficients of 2-8 Mm^{-1} in the lower layer (up to 2.5 km height) and 1-7 Mm^{-1} in the lofted layer above 3 km height are in good agreement with CALIPSO lidar observations (Di Biagio et al., 2018; Yang et al., 2020). Di Biagio et al. (2018) showed 14-day mean and layer mean values of 2-8 Mm^{-1} (0-2 km layer), 2-10 Mm^{-1} (2-5 km), and 1-2 Mm^{-1} (5-10 km layer) measured in the area from 5-25°E (north of Svalbard) and 80-82°N in February and March 2015.

https://doi.org/10.5194/acp-2020-1271
Preprint. Discussion started: 29 December 2020

Atmospheric Chemistry and Physics Discussions

Yang et al. (2020) analyzed 13 years of CALIPSO observations (June 2006 to December 2019) for the Arctic (entire area from 65°N to 81.8°N) and found seasonal mean extinction values ranging from 4-8 Mm^{-1} for the height range from 2-6 km and 4-10 Mm^{-1} for the height range from 6-10 km for autumn season, and 2-4 Mm^{-1} for the height range from 2-6 km and around 2 Mm^{-1} for the height range from 6-10 km for the winter season.

It should be mentioned at the end that, in contrast to Polly, the CALIPSO lidar is a standard backscatter lidar and needs to assume an appropriate lidar ratio in the conversion of the backscatter profiles into respective extinction coefficient profiles. Lidar ratios are between 40–70 sr in the CALIPSO data analysis of Arctic observations. Thus, the MOSAiC Polly data analysis will provide valuable lidar-ratio information for CALIPSO lidar studies of Arctic aerosols. It is planned to analyze all favorable MOSAiC lidar observations without fog and low-level clouds to obtain a seasonally and height-resolved aerosol data set in terms of backscatter, extinction, lidar ratio and depolarization ratio profiles for the Central Arctic.

3.3 Mixed-phase cloud evolution in Arctic haze

The final two subsections give an overview of aerosol-cloud interaction studies that can be performed by using the MOSAiC remote sensing data base. We begin with a mixed-phase-cloud study and continue in Sect. 3.4 with a case of cirrus evolution in the smoke layer above 8 km height. Persistent mixed-phase clouds with rather constant thermodynamic, micro-, and macrophysical properties have been observed over hours, in few cases over even more than 40 hours, especially during the MOSAiC winter half year. Because of their sensitive influence on radiative transfer and the water cycle they have been in the focus of research since more than 15 years (Verlinde et al., 2007; Morrison et al., 2012; Paukert and Hoose, 2014; Loewe et al., 2017; Andronache, 2018; Eirund et al., 2019). However, because of the complexity of influencing meteorological and aerosol aspects, there are still many open questions concerning their long lifetime, especially of the longevity of liquid-water layers and thus of water droplets in the presence of ice crystals. MOSAiC will contribute to this research field by means of combined lidar and radar observations.

In order to better understand the role of aerosol particles in cloud evolution processes we need to combine methods that allow us to measure or retrieve the cloud-relevant aerosol parameters, i.e., the cloud condensation nucleus concentration (CCNC) and ice-nucleating particle concentration (INPC) in the aerosol around the developing cloud layer, together with the cloud droplet number concentration (CDNC) and ice crystal number concentration (ICNC) in the observed cloud layers. In the following, we introduce two recently developed concepts to investigate aerosol-cloud interaction solely based on active remote sensing and explain how we derive the required information of CCNC, INPC, CDNC, and ICNC.

The mixed-phase cloud system, studied here, was shown in Fig. 3e-f. The altocumulus layer was present over the Polarstern for nine hours. Favorable conditions with cloud top temperatures around -28.5°C at 2.6 km height (at 03:00 UTC) were given for heterogeneous ice formation via immersion freezing, i.e., ice nucleation on INPs immersed in the water droplets. After nucleation, the ice crystals grew fast to sizes of 50–100 μm within minutes (Bailey and Hallett, 2012) and immediately started falling out of the altocumulus layer. The ice crystals partly evaporated on the way down, but partly reached the ground as precipitation.

https://doi.org/10.5194/acp-2020-1271
Preprint. Discussion started: 29 December 2020

Atmospheric Chemistry and Physics Discussions

The reasons for the longevity of the shallow cloud top layer mostly consisting of liquid-water droplets are continuously occurring updrafts which permanently cause water supersaturation in the liquid-water layer and droplet nucleation (Ansmann et al., 2009) so that the liquid-water cloud layer can never become completely glaciated. As discussed below in detail, there were always 20-200 droplets per cm^3 in the altocumulus top layer, but only 0.1 to 1 ice crystals per liter, i.e., the droplet-to-crystal number ratio was of the order of 20000 to 200000 and thus too high to convert the liquid water layer into an ice cloud by heterogeneous ice nucleation and riming processes within seconds to minutes before the next updraft led to new droplet formation.

We analyzed the dual-FOV polarization lidar observations of the liquid-water cloud layer. The results are shown in Fig. 11. The applied dual-FOV polarization lidar technique was recently introduced (Jimenez et al., 2020a, b) and successfully tested in the case of water cloud experiments in southern Chile. The new method was originally designed for pure liquid-water cloud observations but can be applied to mixed-phase clouds as long as backscattering by ice crystals is negligible compared to droplet backscattering in the droplet-dominated cloud top layer. This condition holds here with ice crystal backscatter coefficients of 5-10 Mm^{-1} sr^{-1} in the virga and thus also in the cloud top layer and droplet backscatter coefficients of the order of 700 Mm^{-1} sr^{-1}.

As can be seen in seen Fig. 11, the CDNC values were about 20 cm^{-3} in the beginning and around 100 cm^{-3} later on. Obviously, updraft velocity was weak and correspondingly water super saturation levels were below 0.2% so that fewer particles were activated to become cloud droplets as predicted (CCNC values in Fig. 12). Later on, the updrafts became obviously stronger, and supersaturation levels exceeded 0.2% so that more CCN nucleated cloud droplets as predicted by the retrieved CCNC values. With increasing CDNC the effective radius (characterizing the typical droplet size) decreased and vice versa for constant water vapor conditions. The cloud extinction coefficient showed typical values from 10-20 km^{-1} most of the time in the droplet-dominated cloud layer.

CCNC was estimated from the particle extinction coefficient profile measured with lidar before the altocumulus appeared over the lidar site. The particle extinction profile is shown in Fig. 12. The conversion of extinction coefficients into CCN number concentration (for an assumed water supersaturation level of 0.2% during droplet nucleation) is performed by means of method given in Mamouri and Ansmann (2016). We assumed central European haze conditions (Leipzig aerosol conditions) in this conversion (leading to the higher CCNC values in Fig. 12) and aged Arctic haze conditions with less small particles (leading to the lower CCNC values). In this way we estimated CCN concentrations of about 30-70 cm^{-3} with an uncertainty of a factor of 2.

Regarding a closure study of the ice phase, we computed INP concentrations first, again starting from the aerosol extinction profile in Fig. 12. Soot and mineral dust particles are good candidates to serve as INPs. However, soot is an inefficient INP type in the case of immersion freezing at temperatures $> -30°C$ (Kanji et al., 2020; Schill et al., 2020). Dust is left as potential INP. Our polarization lidar observations indicated the presence of a dust fraction of 3-10% according to the slightly enhanced particle depolarization ratio (not shown) above 2 km height, which is in good agreement with studies of Di Biagio et al. (2018) and Yang et al. (2020), who analyzed spaceborne and ground-based lidar observations in combination with backward trajectory analysis and concluded that mineral dust always contributes to the long-transported continental aerosol mixtures in the lower

https://doi.org/10.5194/acp-2020-1271
Preprint. Discussion started: 29 December 2020

Atmospheric Chemistry and Physics Discussions

and middle free troposphere in the Arctic. We used the INP parameterization scheme of DeMott et al. (2010) to estimate the dust INP concentration for immersion freezing. Here, the particle number concentration n_{250} of dust particles with diameters $>$ 500 nm is an input parameter and obtained from the respective lidar observation of the extinction coefficient in Fig. 12 and by assuming a dust fraction of 3-10% in the conversion of the extinction profile into the n_{250} profil (Mamouri and Ansmann, 2016). The retrieval finally yields INPC values in the range from 0.1-0.5 L^{-1} for the altocumulus top temperature of $-28.5°C$.

To obtain also an estimate for ICNC, we combined lidar observations of the 532 nm extinction coefficient in the first strong ice virga zone (4:00-5:00 UTC) below the liquid-water cloud layer, radar reflectivity (8 mm wavelength) and Doppler information on the ice crystal fall speed spectrum in the virga from the AMF-1 KAZR (Ka-band zenith-pointing radar) (ARM-MOSAiC, 2020) with comprehensive model simulations of the lidar and radar observations as a function of ice crystal number concentration, size distribution, and shape (Bühl et al., 2019). The match between simulations and observations provide the range of retrieved ICNC values. In the case of the mixed-phase cloud we obtain 0.1-1.0 ice crystals per liter. The retrieval uncertainty allows us to provide the order of magnitude of ICNC only.

All obtained numbers for the aerosol and cloud particle number concentrations are shown in Fig. 13 together with the relative-humidity field obtained from the Raman lidar water-vapor mixing ratio observations (combined with radiosonde temperature measurements). The relative-humidity height time display in Fig. 13b indicates that the altocumulus layer developed in a moist air mass and was present over the Polarstern until a dry air mass approached, leading to a strong decrease in relative humidity and dissolution of the stratiform cloud deck. As a result of strong ice crystal evaporation in the virga zone, the relative humidity increased strongly below the liquid-water cloud deck after 3:00 UTC and caused reduced crystal evaporation later on in the virga zone so that ice crystals could partly reached the ground as precipitation.

The good match between CCNC and CDNC (liquid-water cloud closure) and between INPC and ICNC (ice cloud closure, see numbers in Fig. 13a) during the early phase of the altocumulus development indicates that the aerosol particles controlled the cloud properties and thus had a strong influence of the evolution of the observed altocumulus cloud system as long as the humidity conditions were favorable. It should be emphasized that such a closure study with consistent findings is only possible if primary ice and droplet nucleation dominates and secondary ice formation, ice breakup processes, crystal-crystal collision and aggregation processes, as well as droplet collision and coagulation, and strong mixing and entrainment processes are absent. As part of the MOSAiC data analysis, we plan to analyze many winter as well as summer altocumulus events and thus cloud formation under contrasting aerosol conditions to obtain an improved view on the role of long-transported aged aerosol pollution on the evolution of mixed-phase clouds in the high Arctic.

3.4 Cirrus evolution in the UTLS wildfire smoke layer

MOSAiC offers the unique opportunity to learn more about the role of wildfire smoke layers on the evolution of Arctic cirrus. A large number of cirrus fields developed in the smoke layer in the upper troposphere during the winter half year (on about 70-90 days in the 7-month period from October to April). Organic aerosol (OA, the main aersol component in wildfire aerosol) is besides dust and marine particles ubiquitous in the atmosphere. However, in contrast to dust and marine particles the INP potential of smoke particles is not well known, in particular for cirrus formation conditions. Scarce field data are

https://doi.org/10.5194/acp-2020-1271
Preprint. Discussion started: 29 December 2020


Atmospheric Chemistry and Physics Discussions

the main reason for the lack of clarity and knowledge. An overview and summary of organic particles, their microphysical, morphological, chemical, and cloud-relevant properties, and their potential role in the atmospheric (climate) system can be found in the review article of Knopf et al. (2018).

Complications in our understanding arises due to the fact that OA particles can occur as glassy, semi-glassy and liquid particles as a function of temperature and relative humidity, and thus can trigger deposition nucleation (as glassy particles), immersion freezing (as semi-glassy particles), and homogeneous freezing (when liquid) (Koop et al., 2000, 2011; Berkemeier et al., 2014; Wang et al., 2012; Knopf et al., 2018). Aerosol particles serving as INPs usually provide an insoluble, solid surface that can facilitate the freezing of water. Deposition ice nucleation is defined as ice formation occurring on the INP surface by water vapor deposition from the supersaturated gas phase. When the supercooled smoke particle takes up water or its shell deliquesces, immersion freezing can proceed, where the INP immersed in an aqueous solution can initiate freezing. Finally, if the smoke particle become completely liquid (and contain no solid soot fragments), homogeneous freezing will take place at temperatures below 235 K. However, in reality, at given air mass lifting conditions, the ice nucleation process can be very complex. The time that solid organic material (OM) needs for transition to a more liquid state, termed as humidity-induced amorphous deliquescence, can range from several minutes to days at temperatures low enough for ice formation (Mikhailov et al., 2009; Berkemeier et al., 2014; Knopf et al., 2018). Thus the phase change (as function of T and RH) can be longer than typical cloud activation time periods (governed by the updraft velocity), potentially inhibiting full deliquescence and allowing the OA or the organic coating to serve as INP. When amorphous OA or OM are involved in ice nucleation, the condensed-phase diffusion processes within OA particles will most probably govern the ice nucleation pathway (Wang et al., 2012).

To demonstrate that the observed wildfire smoke particle were able to control cirrus evolution and life time we present the results of a first MOSAiC case study here. The observation is from 6 December 2019 (Fig. 3c and d). HYSPLIT backward trajectory analysis (for arrival heights at 8-9.5 km and arrival times of 6, 10, and 14 UTC) indicate air mass transport within the Arctic at latitudes $> 70°$N and heights between 7-10 km during the last seven days before crossing the MOSAiC field site (86°N, 122°E). The air masses originated from the remote northern Pacific, and transported water vapor and probably unpolluted marine air. The ascent of the moist air masses occurred 8-10 days before arrival in the Central Arctic. During the 7-day travel in the Arctic the Pacific airmass mixed with the smoke above 7 km. These smoke particles then served as ice nuclei when cirrus formed after further lifting. Remaining marine particles may have served as INPs as well, but are inefficient INPs (McCluskey et al., 2018; Haarig et al., 2019).

The full cirrus lifetime was about 36 hours. The wildfire smoke is best visible as a light blue layer above 9.3 km height, i.e., above the main cirrus layer, between 6:00 and 12:00 UTC in Fig. 3c. This part of the smoke layer (above 9.3 km) can be regarded as the main reservoir of INPs. The bow-like feature of the lower boundary of the extended virga zone (between 00:00 to 18:00 UTC) was caused by a high pressure ridge (with dome-like temporal evolution of the influenced height range). The ridge crossed RV Polarstern during this day and was characterized by a warmer and very dry air mass in the lowest few kilometers of the troposphere. After entering this dry air mass the ice crystals immediately evaporated.

The data analysis with respect to ice nucleation on smoke particles is explained in Fig. 14 and 15. We applied the water-activity-based immersion freezing model (ABIFM) that allows predicting of immersion freezing under cirrus conditions (Knopf

https://doi.org/10.5194/acp-2020-1271
Preprint. Discussion started: 29 December 2020

Atmospheric Chemistry and Physics Discussions

and Alpert, 2013). In addition, we used the parameterization for deposition ice nucleation (DIN) of Wang and Knopf (2011). Ice nucleation from the water vapor phase is denoted as deposition nucleation. Figure 14a shows the cirrus layers observed from 6-12 UTC (red) and 12:30-13:30 UTC (blue) on 6 December 2019 and the temperature and relative humidity profiles of radiosondes launched aboard Polarstern at 5, 11 and 17 UTC on this day (Fig. 14b).

Whereas the parameterization for DIN uses ambient temperature and humidity (i.e., ice supersaturation S_{i}, see Fig. 14c) to derive a nucleation rate coefficient that is used to calculate INPC, ABIFM requires the derivation of the water-activity criterion Δa_{w} (Koop et al., 2000). Δa_{w} describes the difference between the ice melting conditions (melting temperature) and the observed freezing conditions in terms of temperature and humidity. Homogeneous ice nucleation is characterized by Δa_{w} 0.313 (Knopf and Rigg, 2011), and smaller values of Δa_{w} are then characteristic for immersion freezing (Knopf and Alpert, 2013). As can be seen, Δa_{w} takes values of 0.1-0.2 according to the radiosonde observations. However, Δa_{w} values of 0.25-0.29 are needed (indicated by the short vertical lines in Fig. 14c) to start efficient ice nucleation on smoke particles (Knopf and Alpert, 2013). Leonardite, a humic acid also present in biomass burning aerosol serves as surrogate INP material. Also in the case of DIN, laboratory results for Leonardite are used (Wang and Knopf, 2011). Ice supersaturation conditions are usually given or produced during updrafts (e.g., during the ascending period of a gravity wave) that could, in principle, be detected and measured with the AMF-1 Doppler radar.

It is noteworthy to mention here, that equilibrium at ice supersaturation conditions as observed in the extended virga zone over the whole day (Fig. 14c) is a sign for a low crystal number concentration ($<$35 L^{-1}) (Murray et al., 2010). Such a low amount of ice crystals is not able to quench the supersaturation which is in turn indicative for heterogeneous ice nucleation. Homogeneous freezing would produce crystal concentrations of $>$500 L^{-1} so that equilibrium at ice saturation level would occur within a short time period.

Figure 15 provides an overview of all retrieval products necessary to evaluate the potential of smoke particles to serve as INP. We follow here the strategy of the ICNC-INPC closure study (Ansmann et al., 2019). The lidar-radar combination (with TROPOS lidar and the 35-GHz AMF-1 cloud radar KAZR) delivers ICNC values (n_{ICE}) (Bühl et al., 2019) as given in Fig. 15a and c. The best and most trustworthy radar observations are usually taken in the lower part of the cloud deck where ice crystals are large and thus radar reflectivity is usually very strong and accurate. However, we have to keep in mind that these ICNC values may be lower than the ones at cloud top caused by crystal-crystal collision and aggregation processes (Mitchell et al., 2018). Other ICNC influencing effects, e.g., secondary ice formation can be ignored in the case of cold cirrus clouds (Field et al., 2006; Korolev and Leisner, 2020). From the aerosol lidar observations (at cloud free conditions, for example on 2 and 7 December) we can derive the range (or amount) of available smoke particles and related particle surface area s (in Fig. 15b, upper axis). In this figure, the number concentration of large smoke particles n_{250} (with radii > 250 nm, lower axis) is shown as well. This number indicates the overall reservoir of favorable INPs (Ansmann et al., 2020). The surface area s is the smoke input parameter in the estimation of the INPC value ($n_{\mathrm{INP,D}}$, for deposition nucleation and $n_{\mathrm{INP,I}}$ for immersion freezing). The INP parameterization overview is given in Ansmann et al. (2020).

As mentioned, ice nucleation occurs during updraft periods, more precisely when a certain (threshold) supersaturation level is exceeded. And the length of the supersaturation period determines the overall nucleation rate and the number of nucleated

https://doi.org/10.5194/acp-2020-1271
Preprint. Discussion started: 29 December 2020


Atmospheric Chemistry and Physics Discussions

crystals. 600 seconds of updraft duration and values of 0.225-0.250 for the water activity criterion Δa_{w} are considered in Fig. 15c. 600 s may represent here a typical time period of the lifting phase of a gravity wave. As can be seen the n_{ICE} and $n_{\mathrm{INP,I}}$ values (blue and red bars) are in the same range of values which suggests that organic particles may be able to control the evolution of the cirrus layer via the immersion freezing mode (i.e., when the smoke particles have a liquid shell). The impact of deposition INP $n_{\mathrm{INP,D}}$ (cyan and orange bars) is comparably weak in this example. We assume here that smoke particles have a solid core (containing black carbon) and a shell of organic material (here Leonardite is assumed) which can liquefy at certain temperature and humidity conditions. The deposition-nucleation and immersion-freezing ability depends on the surface material of the smoke particles. In the MOSAiC data analysis later on we will consider different organic substances (more details in Knopf and Alpert (2013)). It has been shown that humic and fulvic matter can act as deposition nucleation and immersion freezing INPs (Wang and Knopf, 2011; Rigg et al., 2013; Knopf and Alpert, 2013; Knopf et al., 2018). Furthermore, these macromolecules can undergo amorphous phase transition under typical tropospheric conditions (Wang et al., 2012; Slade et al., 2017) similar to the processes we assume the organic coating of the smoke particles experiences.

To sum up, heterogeneous ice nucleation is a complex process, especially in the case of organic aerosol particles. However, the successful closure, indicated by a reasonable match between $n_{\mathrm{INP,I}}$ and n_{ICE}, indicates that the wildfire smoke was able to trigger cirrus formation (before homogeneous freezing can take place on stratospheric background or even liquid smoke particles) and control of the further evolution of the ice cloud system. It is clear that many more closure studies are needed to obtain a statistically trustworthy view on smoke and the role in cirrus nucleation. The respective extended data analysis will be part of our MOSAiC data analysis.

4 Conclusion and outlook

The goal of this introductory article was to provide an overview of the capabilities of modern lidar methods to contribute to Arctic research of aerosols and clouds. Continuous observations were performed mostly at latitudes $> 85°$N during the MOSAiC year from September 2019 to October 2020.

The highlight of our observations was the detection of the long lasting UTLS wildfire smoke layer which was present over the North Pole region for seven month until spring. More details to the smoke layer and the potential impact on the record-breaking ozone reduction is given by Ohneiser et al. (2021). Besides the smoke, we presented two days with typical Artcis haze layering features and properties. The results agree well with foregoing studies, e.g., performed in the framework of POLARCAT-IPY and ARCTAS.

Our research focus is on aerosol-cloud interaction, especially on ice nucleation in mixed-phase clouds and cirrus. We developed new techniques, data analysis concepts, and closure experiments and applied them for the first time to Arctic cloud studies. The successful closure experiments corroborate that aerosol particles are able to control cloud evolution and cloud microphysical properties. In the cirrus case study, homogeneous freezing was not needed to explain the formation of the cirrus deck within the wildfire smoke layers.

https://doi.org/10.5194/acp-2020-1271
Preprint. Discussion started: 29 December 2020


Atmospheric Chemistry and Physics Discussions

As an outlook, we will analyze the one-year data set to characterize the annual cycle of aerosol and cloud conditions and will contrast winter with summer conditions especially regarding aerosol-cloud interaction. Aerosol conditions during winter and early spring are very different from the ones during the summer and early autumn season and thus the impact of aerosol particles on mixed-phase cloud and cirrus evolution should be different as well. The later MOSAiC observations from July to October 2020 however showed that smoke layers were again frequently present in the Central Arctic because of the strong fire activity in Siberia and North America in the summer of 2020.

5 Data availability

Polly lidar observations (level 0 data, measured signals) are in the PollyNET data base (PollyNET, 2020) with quicklooks at http://picasso.tropos.de. All the analysis products are available at TROPOS upon request (polly@tropos.de). The AMF-1 cloud radar data are provided by the ARM MOSAiC user facility (ARM-MOSAiC, 2020). In addition, all MOSAiC consortium members have early access to the data via the MOSAiC Central Storage (MCS) system before the data become publicly released on 1 January 2023. The radiosonde data are currently as well available via the MCS. PANGAEA is the primary long-term archive for the MOSAiC data set. KAZR data are available via the ARM data achieve (https://adc.arm.gov/discovery/).

6 Author contributions

The paper was written by RE and AA with contributions (data analysis) from KO, HB, CJ, JB, HGe, MH, SD, MM, IV, and PS. The co-authors HGr, MR, JH, and DA as well as RE took care of the lidar observations aboard Polarstern during the MOSAiC year. CJ and RW implemented and tested the new dual-FOV polarization lidar channels. UW and MA were involved in the data interpretation and discussions of the observations.

7 Competing interests

The authors declare that they have no conflict of interest.

8 Financial support

The data was produced as part of the international Multidisciplinary drifting Observatory for the Study of the Arctic Climate (MOSAiC) with the tag MOSAiC20192020 and Project ID AWI_PS122_00. This project has also received funding from the European Union's Horizon 2020 research and innovation program ACTRIS-2 Integrating Activities (H2020-INFRAIA-2014 - 2015, grant agreement no. 654109). We gratefully acknowledge the funding by the Deutsche Forschungsgemeinschaft (DFG,German Research Foundation) – project no. 268020496 - TRR 172, within the Transregional Collaborative Research Center "ArctiC Amplification: Climate Relevant Atmospheric andSurfaCe Processes, and Feedback Mechanisms (AC)3". The

https://doi.org/10.5194/acp-2020-1271
Preprint. Discussion started: 29 December 2020

development of the lidar inversion algorithm used to analyze Polly data was supported by the Russian Science Foundation (project no. 16-17-10241).

The publication of this article was funded by the Open Access Fund of the Leibniz Association.

Acknowledgements. We are grateful to the MOSAiC teams and the RV Polarstern crew for their perfect logistical support. Cloud radar data was provided by the US Department of Energy's Atmospheric Radiation Measurement Program. We further thank the entire radiosonde team, especially AWI, DWD, ARM, Jürgen (Egon) Graeser, and all volunteers for their enormous efforts of producing the exemplary and uninterrupted six-hourly dataset in the full MOSAiC year.

https://doi.org/10.5194/acp-2020-1271
Preprint. Discussion started: 29 December 2020

Atmospheric Chemistry and Physics Discussions

References

Abbatt, J. P. D., Leaitch, W. R., Aliabadi, A. A., Bertram, A. K., Blanchet, J.-P., Boivin-Rioux, A., Bozem, H., Burkart, J., Chang, R. Y. W., Charette, J., Chaubey, J. P., Christensen, R. J., Cirisan, A., Collins, D. B., Croft, B., Dionne, J., Evans, G. J., Fletcher, C. G., Galí, M., Ghahremaninezhad, R., Girard, E., Gong, W., Gosselin, M., Gourdal, M., Hanna, S. J., Hayashida, H., Herber, A. B., Hesaraki, S., Hoor, P., Huang, L., Hussherr, R., Irish, V. E., Keita, S. A., Kodros, J. K., Köllner, F., Kolonjari, F., Kunkel, D., Ladino, L. A., Law, K., Levasseur, M., Libois, Q., Liggio, J., Lizotte, M., Macdonald, K. M., Mahmood, R., Martin, R. V., Mason, R. H., Miller, L. A., Moravek, A., Mortenson, E., Mungall, E. L., Murphy, J. G., Namazi, M., Norman, A.-L., O'Neill, N. T., Pierce, J. R., Russell, L. M., Schneider, J., Schulz, H., Sharma, S., Si, M., Staebler, R. M., Steiner, N. S., Thomas, J. L., von Salzen, K., Wentzell, J. J. B., Willis, M. D., Wentworth, G. R., Xu, J.-W., and Yakobi-Hancock, J. D.: Overview paper: New insights into aerosol and climate in the Arctic, Atmos. Chem. Phys., 19, 2527-2560, https://doi.org/10.5194/acp-19-2527-2019, 2019.

Achtert, P., and Tesche, M.: Assessing lidar-based classification schemes for polar stratospheric clouds based on 16 years of measurements at Esrange, Sweden, J. Geophys. Res. Atmos., 119, 1386– 1405, doi:10.1002/2013JD020355, 2014.

ACTRIS: Aerosols, Clouds and Trace gases Research InfraStructure home page, avaialble at https://www.actris.eu/, last access: 20 October, 2020.

Andronache, C. (Ed.): Mixed-Phase Clouds, Elsevier, 1 Edn., the Netherlands, UK, USA, 2018.

Ansmann, A., Tesche, M., Seifert, P., Althausen, D., Engelmann, R., Fruntke, J., Wandinger, U., Mattis, I., and Müller, D.: Evolution of the ice phase in tropical altocumulus: SAMUM lidar observations over Cape Verde, J. Geophys. Res., 114, D17208, https://doi.org/10.1029/2008JD011659, 2009.

Ansmann, A., Baars, H., Chudnovsky, A., Mattis, I., Veselovskii, I., Haarig, M., Seifert, P., Engelmann, R., and Wandinger, U.: Extreme levels of Canadian wildfire smoke in the stratosphere over central Europe on 21–22 August 2017, Atmos. Chem. Phys., 18, 11831-11845, https://doi.org/10.5194/acp-18-11831-2018, 2018.

Ansmann, A., Mamouri, R.-E., Bühl, J., Seifert, P., Engelmann, R., Hofer, J., Nisantzi, A., Atkinson, J. D., Kanji, Z. A., Sierau, B., Vrekoussis, M., and Sciare, J.: Ice-nucleating particle versus ice crystal number concentrationin altocumulus and cirrus layers embedded in Saharan dust:a closure study, Atmos. Chem. Phys., 19, 15087–15115, https://doi.org/10.5194/acp-19-15087-2019, 2019.

Ansmann, A., Ohneiser, K., Mamouri, R.-E., Knopf, D. A., Veselovskii, I., Baars, H., Engelmann, R., Foth, A., Jimenez, C., Seifert, P., and Barja, B.: Tropospheric and stratospheric wildfire smoke profiling with lidar: Mass, surface area, CCN and INP retrieval, Atmos. Chem. Phys. Discuss., https://doi.org/10.5194/acp-2020-1093, in review, 2020.

ARM: Atmospheric Radiation Measurement (ARM) mobile facility homepage, available at https://www.arm.gov/capabilities/observatories/amf, last access: 20 October, 2020.

ARM-MOSAiC: Atmospheric Radiation Measurement (ARM) user facility, 2019, updated hourly, Ka ARM Zenith Radar (KAZRCFRGE), 2019-10-11 to 2020-09-20, ARM Mobile Facility (MOS) MOSAIC (Drifting Obs - Study of Arctic Climate), AMF2 (M1), compiled by I. Lindenmaier, D. Nelson, B. Isom, J. Hardin, A. Matthews, T. Wendler, and V. Castro, ARM Data Center, last access: 13 December, 2020.

Avery, M. A., Ryan, R. A., Getzewich, B. J., Vaughan, M. A., Winker, D. M., Hu, Y., Garnier, A., Pelon, J., and Verhappen, C. A.: CALIOP V4 cloud thermodynamic phase assignment and the impact of near-nadir viewing angles, Atmos. Meas. Tech., 13, 4539–4563, https://doi.org/10.5194/amt-13-4539-2020, 2020.

https://doi.org/10.5194/acp-2020-1271
Preprint. Discussion started: 29 December 2020

Baars, H., Ansmann, A., Althausen, D., Engelmann, R., Heese, B., Müller, D., Artaxo, P., Paixao, M., Pauliquevis, T., and Souza, R.: Aerosol profiling with lidar in the Amazon Basin during the wet and dry season, J. Geophys. Res., 117, D21201, doi:10.1029/2012JD018338, 2012.

Baars, H., Kanitz, T., Engelmann, R., Althausen, D., Heese, B., Komppula, M., Preißler, J., Tesche, M., Ansmann, A., Wandinger, U., Lim, J.-H., Ahn, J. Y., Stachlewska, I. S., Amiridis, V., Marinou, E., Seifert, P., Hofer, J., Skupin, A., Schneider, F., Bohlmann, S., Foth, A., Bley, S., Pfüller, A., Giannakaki, E., Lihavainen, H., Viisanen, Y., Hooda, R. K., Pereira, S. N., Bortoli, D., Wagner, F., Mattis, I., Janicka, L., Markowicz, K. M., Achtert, P., Artaxo, P., Pauliquevis, T., Souza, R. A. F., Sharma, V. P., van Zyl, P. G., Beukes, J. P., Sun, J., Rohwer, E. G., Deng, R., Mamouri, R.-E., and Zamorano, F.: An overview of the first decade of PollyNET: an emerging network of automated Raman-polarization lidars for continuous aerosol profiling, Atmos. Chem. Phys., 16, 5111-5137, https://doi.org/10.5194/acp-16-5111-2016, 2016.

Baars, H., Ansmann, A., Ohneiser, K., Haarig, M., Engelmann, R., Althausen, D., Hanssen, I., Gausa, M., Pietruczuk, A., Szkop, A., Stachlewska, I. S., Wang, D., Reichardt, J., Skupin, A., Mattis, I., Trickl, T., Vogelmann, H., Navas-Guzmán, F., Haefele, A., Acheson, K., Ruth, A. A., Tatarov, B., Müller, D., Hu, Q., Podvin, T., Goloub, P., Veselovskii, I., Pietras, C., Haeffelin, M., Fréville, P., Sicard, M., Comerón, A., Fernández García, A. J., Molero Menéndez, F., Córdoba-Jabonero, C., Guerrero-Rascado, J. L., Alados-Arboledas, L., Bortoli, D., Costa, M. J., Dionisi, D., Liberti, G. L., Wang, X., Sannino, A., Papagiannopoulos, N., Boselli, A., Mona, L., D'Amico, G., Romano, S., Perrone, M. R., Belegante, L., Nicolae, D., Grigorov, I., Gialitaki, A., Amiridis, V., Soupiona, O., Papayannis, A., Mamouri, R.-E., Nisantzi, A., Heese, B., Hofer, J., Schechner, Y. Y., Wandinger, U., and Pappalardo, G.: The unprecedented 2017–2018 stratospheric smoke event: decay phase and aerosol properties observed with the EARLINET, Atmos. Chem. Phys., 19, 15183–15198, https://doi.org/10.5194/acp-19-15183-2019, 2019.

Baars, H., Herzog, A., Heese, B., Ohneiser, K., Hanbuch, K., Hofer, J., Yin, Z., Engelmann, R., and Wandinger, U.: Validation of Aeolus wind products above the Atlantic Ocean, Atmos. Meas. Tech., 13, 6007–6024, https://doi.org/10.5194/amt-13-6007-2020, 2020.

Bailey, M., and Hallett, J.: Ice Crystal Linear Growth Rates from −20° to −70°C: Confirmation from Wave Cloud Studies, J. Atmos. Sci., 69, 390-402, https://doi.org/10.1175/JAS-D-11-035.1, 2012

Berkemeier, T., Shiraiwa, M., Pöschl, U., and Koop, T.: Competition between water uptake and ice nucleation by glassy organic aerosol particles, Atmos. Chem. Phys., 14, 12513–12531, https://doi.org/10.5194/acp-14-12513-2014, 2014.

Boers, R., de Laat, A. T., Stein Zweers, D. C., and Dirksen, R. J.: Lifting potential of solar-heated aerosol layers, Geophys. Res. Lett., 37, L24802, doi:10.1029/2010GL045171, 2010.

Bohlmann, S., Baars, H., Radenz, M., Engelmann, R., and Macke, A.: Ship-borne aerosol profiling with lidar over the Atlantic Ocean: from pure marine conditions to complex dust–smoke mixtures, Atmos. Chem. Phys., 18, 9661-9679, https://doi.org/10.5194/acp-18-9661-2018, 2018.

Bourassa, A. E., Rieger, L. A., Zawada, D. J., Khaykin, S., Thomason, L. W., and Degenstein, D. A.: Satellite limb observations of unprecedented forest fire aerosol in the stratosphere. J. Geophys. Res. - Atmospheres, 124, 9510–9519. https://doi.org/10.1029/2019JD030607, 2019.

Bozem, H., Hoor, P., Kunkel, D., Köllner, F., Schneider, J., Herber, A., Schulz, H., Leaitch, W. R., Aliabadi, A. A., Willis, M. D., Burkart, J., and Abbatt, J. P. D.: Characterization of transport regimes and the polar dome during Arctic spring and summer using in situ aircraft measurements, Atmos. Chem. Phys., 19, 15049–15071, https://doi.org/10.5194/acp-19-15049-2019, 2019.

Bühl, J., Seifert, P., Radenz, M., Baars, H., and Ansmann, A.: Ice crystal number concentration from lidar, cloud radar and radar wind profiler measurements, Atmos. Meas. Tech., 12, 6601–6617, https://doi.org/10.5194/amt-12-6601-2019, 2019.

https://doi.org/10.5194/acp-2020-1271
Preprint. Discussion started: 29 December 2020

Atmospheric Chemistry and Physics Discussions

CALIPSO: Cloud–Aerosol Lidar and Infrared Pathfinder Satellite Observation Lidar Level 2 data, height-time displays of attenuated backscatter, available at https://www-calipso.larc.nasa.gov/products/lidar/browse_images/std_v4_index.php, last access: 20 October, 2020a.

CALIPSO: Cloud–Aerosol Lidar and Infrared Pathfinder Satellite Observation Lidar Level 2 data, particle backscatter profiles, available at https://search.earthdata.nasa.gov/search?fp=CALIPSO&fi=CALIOP, last access: 20 October, 2020b.

Dahlkötter, F., Gysel, M., Sauer, D., Minikin, A., Baumann, R., Seifert, P., Ansmann, A., Fromm, M., Voigt, C., and Weinzierl, B.: The Pagami Creek smoke plume after long-range transport to the upper troposphere over Europe – aerosol properties and black carbon mixing state, Atmos. Chem. Phys., 14, 6111–6137, https://doi.org/10.5194/acp-14-6111-2014, 2014.

Dai, G., Althausen, D., Hofer, J., Engelmann, R., Seifert, P., Bühl, J., Mamouri, R.-E., Wu, S., and Ansmann, A.: Calibration of Raman lidar water vapor profiles by means of AERONET photometer observations and GDAS meteorological data, Atmos. Meas. Tech., 11, 2735–2748, https://doi.org/10.5194/amt-11-2735-2018, 2018.

DeLand, M. T., Bhartia, P. K., Kramarova, N., and Chen, Z.: OMPS LP observations of PSC variability during the NH 2019-2020 season, Geophys. Res. Lett., 47, e2020GL090216. https://doi.org/10.1029/2020GL090216, 2020.

DeMott, P. J., Prenni, A. J., Liu, X., Kreidenweis, S. M., Petters, M. D., Twohy, C. H., Richardson, M. S., Eidhammer, T., and Rogers, D. C.: Predicting global atmospheric ice nuclei distributions and their impacts on climate, Proc. Natl. Acad. Sci. USA, 107, 11217–11222, doi:10.1073/pnas.0910818107, 2010.

de Laat, A. T. J., Stein Zweers, D. C., Boers, R., and Tuinder, O. N. E.: A solar escalator: Observational evidence of the self-lifting of smoke and aerosols by absorption of solar radiation in the February 2009 Australian Black Saturday plume, J. Geophys. Res., 117, D04204, doi:10.1029/2011JD017016, 2012.

Devasthale, A., Tjernström, M. and Omar, A.H.: The vertical distribution of thin features over the Arctic analysed from CALIPSO observations - Part II: Aerosols, Tellus B, 63: 86-95. doi:10.1111/j.1600-0889.2010.00517.x, 2011.

Di Biagio, C., Pelon, J., Ancellet, G., Bazureau, A., and Mariage, V.: Sources, load, vertical distribution, and fate of wintertime aerosols north of Svalbard from combined V4 CALIOP data, ground-based IAOOS lidar observations and trajectory analysis. Journal of Geophysical Research: Atmospheres, 123, 1363– 1383. https://doi.org/10.1002/2017JD027530, 2018.

Di Pierro, M., Jaeglé, L., Eloranta, E. W., and Sharma, S.: Spatial and seasonal distribution of Arctic aerosols observed by the CALIOP satellite instrument (2006–2012), Atmos. Chem. Phys., 13, 7075–7095, https://doi.org/10.5194/acp-13-7075-2013, 2013.

Eirund, G. K., Possner, A., and Lohmann, U.: Response of Arctic mixed-phase clouds to aerosol perturbations under different surface forcings, Atmos. Chem. Phys., 19, 9847–9864, https://doi.org/10.5194/acp-19-9847-2019, 2019.

Eloranta, E., High Spectral Resolution Lidar, in *LIDAR — Range–resolved optical remote sensing of the atmosphere*, C.Weitkamp, ed., Springer, New York (ISBN 0-387-40075-3), 143-163, 2005.

Engelmann, R., Kanitz, T., Baars, H., Heese, B., Althausen, D., Skupin, A., Wandinger, U., Komppula, M., Stachlewska, I. S., Amiridis, V., Marinou, E., Mattis, I., Linné, H., and Ansmann, A.: The automated multiwavelength Raman polarization and water-vapor lidar PollyXT: the neXT generation, Atmos. Meas. Tech., 9, 1767-1784, doi:10.5194/amt-9-1767-2016, 2016.

Fetterer, F., Knowles, K., Meier, W. N., Savoie, M., and Windnagel, A. K.: Sea Ice Index, Version 3, 2017, Monthly Sea Ice Extent. Boulder, Colorado USA. NSIDC: National Snow and Ice Data Center. https://doi.org/10.7265/N5K072F8, accessed 15 July, 2020.

Fiebig, M., Stohl, A., Wendisch, M., Eckhardt, S., and Petzold, A.: Dependence of solar radiative forcing of forest fire aerosol on aging and state of mixture, Atmos. Chem. Phys., 3, 881–891, https://doi.org/10.5194/acp-3-881-2003, 2003.

https://doi.org/10.5194/acp-2020-1271
Preprint. Discussion started: 29 December 2020

Field, P.R., Heymsfield, A. J., and Bansemer, A.: A Test of Ice Self-Collection Kernels Using Aircraft Data, J. Atmos. Sci., 63, 651–666, https://doi.org/10.1175/JAS3653.1, 2006.

Fromm, M. D., and Servranckx, R.: Transport of forest fire smoke above the tropopause by supercell convection, Geophys. Res. Lett., 30, 1542, doi:10.1029/2002GL016820, 2003.

Fromm, M., Shettle, E. P., Fricke, K. H., Ritter, C., Trickl, T., Giehl, H., Gerding, M., Barnes, J. E., O'Neill, M., Massie, S. T., Blum, U., McDermid, I. S., Leblanc, T., and Deshler, T.: Stratospheric impact of the Chisholm pyrocumulonimbus eruption: 2. Vertical profile perspective, J. Geophys. Res., 113, D08203, doi:10.1029/2007JD009147, 2008.

Fromm, M., Lindsey, D. T., Servranckx, R., Yue, G., Trickl, T., Sica, R., Doucet, P., and Godin-Beekmann, S. E.: The untold story of pyrocumulonimbus, B. Am. Meteorol. Soc., 91, 1193–1209, doi:10.1175/2010bams3004.1, 2010.

Gialitaki, A., Tsekeri, A., Amiridis, V., Ceolato, R., Paulien, L., Kampouri, A., Gkikas, A., Solomos, S., Marinou, E., Haarig, M., Baars, H., Ansmann, A., Lapyonok, T., Lopatin, A., Dubovik, O., Groß, S., Wirth, M., Tsichla, M., Tsikoudi, I., and Balis, D.: Is the near-spherical shape the "new black" for smoke?, Atmos. Chem. Phys., 20, 14005–14021, https://doi.org/10.5194/acp-20-14005-2020, 2020.

Grenier, P., Blanchet, J. P., and Munoz-Alpizar, R.: Study of polar thin ice clouds and aerosols seen by CloudSat and CALIPSO during mid-winter 2007, J. Geophys. Res., 114, D09201, doi:10.1029/2008JD010927, 2009.

Griesche, H. J., Seifert, P., Ansmann, A., Baars, H., Barrientos Velasco, C., Bühl, J., Engelmann, R., Radenz, M., Zhenping, Y., and Macke, A.: Application of the shipborne remote sensing supersite OCEANET for profiling of Arctic aerosols and clouds during Polarstern cruise PS106, Atmos. Meas. Tech., 13, 5335–5358, https://doi.org/10.5194/amt-13-5335-2020, 2020a.

Griesche, H. J., Ohneiser, K., Seifert, P., Ansmann, A., and Engelmann, R.: Contrasting ice formation in Arctic clouds: surface coupled vs decoupled clouds, Atmos. Chem. Phys. Discuss., https://doi.org/10.5194/acp-2020-1096, in review, 2020b.

Haarig, M., Ansmann, A., Baars, H., Jimenez, C., Veselovskii, I., Engelmann, R., and Althausen, D.: Depolarization and lidar ratios at 355, 532, and 1064 nm and microphysical properties of aged tropospheric and stratospheric Canadian wildfire smoke, Atmos. Chem. Phys., 18, 11847-11861, https://doi.org/10.5194/acp-18-11847-2018, 2018.

Haarig, M., Walser, A., Ansmann, A., Dollner, M., Althausen, D., Sauer, D., Farrell, D., and Weinzierl, B.: Profiles of cloud condensation nuclei, dust mass concentration, and ice-nucleating-particle-relevant aerosol properties in the Saharan Air Layer over Barbados from polarization lidar and airborne in situ measurements, Atmos. Chem. Phys., 19, 13773–13788, https://doi.org/10.5194/acp-19-13773-2019, 2019.

Hofer, J., Althausen, D., Abdullaev, S. F., Makhmudov, A. N., Nazarov, B. I., Schettler, G., Engelmann, R., Baars, H., Fomba, K. W., Müller, K., Heinold, B., Kandler, K., and Ansmann, A.: Long-term profiling of mineral dust and pollution aerosol with multiwavelength polarization Raman lidar at the Central Asian site of Dushanbe, Tajikistan: case studies, Atmos. Chem. Phys., 17, 14559-14577, https://doi.org/10.5194/acp-17-14559-2017, 2017.

Hofer, J., Ansmann, A., Althausen, D., Engelmann, R., Baars, H., Abdullaev, S. F., and Makhmudov, A. N.: Long-term profiling of aerosol light extinction, particle mass, cloud condensation nuclei, and ice-nucleating particle concentration over Dushanbe, Tajikistan, in Central Asia, Atmos. Chem. Phys., 20, 4695–4711, https://doi.org/10.5194/acp-20-4695-2020, 2020.

Hu, Q., Goloub, P., Veselovskii, I., Bravo-Aranda, J.-A., Popovici, I. E., Podvin, T., Haeffelin, M., Lopatin, A., Dubovik, O., Pietras, C., Huang, X., Torres, B., and Chen, C.: Long-range-transported Canadian smoke plumes in the lower stratosphere over northern France, Atmos. Chem. Phys., 19, 1173-1193, https://doi.org/10.5194/acp-19-1173-2019, 2019.

HYSPLIT: HYbrid Single-Particle Lagrangian Integrated Trajectory model, backward trajectory calculation tool, available at: http://ready.arl.noaa.gov/HYSPLIT_traj.php, last access: 20 October 2020.

https://doi.org/10.5194/acp-2020-1271
Preprint. Discussion started: 29 December 2020

Inness, A., Chabrillat, S., Flemming, J., Huijnen, V., Langenrock, B., Nicolas, J., Polichtchouk, I., and Razingeret, M.: Exceptionally low Arctic stratospheric ozone in spring 2020 as seen in the CAMS reanalysis, Journal of Geophysical Research - Atmospheres, 125, e2020JD033563, https://doi.org/10.1029/2020JD033563, 2020.

Jäger, H., and Deshler, T.: Correction to Lidar backscatter to extinction, mass and area conversions for stratospheric aerosols based on midlatitude balloonborne size distribution measurements, Geophys. Res. Lett., 30, 7, 1382, doi: 10.1029/2003GL017189, 2003.

Jimenez, C., Ansmann, A., Engelmann, R., Donovan, D., Malinka, A., Schmidt, J., Seifert, P., and Wandinger, U.: The dual-field-of-view polarization lidar technique: a new concept in monitoring aerosol effects in liquid-water clouds – theoretical framework, Atmos. Chem. Phys., 20, 15247–15263, https://doi.org/10.5194/acp-20-15247-2020, 2020a.

Jimenez, C., Ansmann, A., Engelmann, R., Donovan, D., Malinka, A., Seifert, P., Wiesen, R., Radenz, M., Yin, Z., Bühl, J., Schmidt, J., Barja, B., and Wandinger, U.: The dual-field-of-view polarization lidar technique: a new concept in monitoring aerosol effects in liquid-water clouds – case studies, Atmos. Chem. Phys., 20, 15265–15284, https://doi.org/10.5194/acp-20-15265-2020, 2020b.

Jouan, C., Pelon, J., Girard, E., Ancellet, G., Blanchet, J. P., and Delanoë, J.: On the relationship between Arctic ice clouds and polluted air masses over the North Slope of Alaska in April 2008, Atmos. Chem. Phys., 14, 1205–1224, https://doi.org/10.5194/acp-14-1205-2014, 2014.

Jouan, C., Girard, E., Pelon, J., Gultepe, I., Delanoë, J., and Blanchet, J. P.: Characterization of Arctic ice cloud properties observed during ISDAC, J. Geophys. Res., 117, D23207, doi:10.1029/2012JD017889, 2012.

Jumelet, J., Klekociuk, A. R., Alexander, S. P., Bekki, S., Hauchecorne, A., Vernier, J. P., Fromm, M., and Keckhut, P.: Detection of aerosols in Antarctica from long-range transport of the 2009 Australian wildfires, Journal of Geophysical Research - Atmospheres, 125, e2020JD032542. https://doi.org/10.1029/2020JD032542, 2020.

Kanitz, T., Seifert, P., Ansmann, A., Engelmann, R., Althausen, D., Casiccia, C., and Rohwer, E. G.: Contrasting the impact of aerosols at northern and southern midlatitudes on heterogeneous ice formation, Geophys. Res. Lett., 38, L17802, doi:10.1029/2011GL048532, 2011.

Kanitz, T., Ansmann, A., Engelmann, R., and Althausen, D.: North-south cross sections of the vertical aerosol distribution over the Atlantic Ocean from multiwavelength Raman/polarization lidar during Polarstern cruises, J. Geophys. Res. Atmos., 118, 2643-2655, doi:10.1002/jgrd.50273, 2013.

Kanji, Z. A., Welti, A., Corbin, J. C., and Mensah, A. A.: Black carbon particles do not matter for immersion mode ice nucleation, Geophysical Research Letters, 46, e2019GL086764, https://doi.org/10.1029/2019GL086764, 2020.

Kablick, G. P., Allen, D. R., Fromm, M. D., and Nedoluha, G. E.: Australian pyroCb smoke generates synoptic-scale stratospheric anticyclones, Geophys. Res. Lett., 47, e2020GL088101. https://doi.org/10.1029/2020GL088101, 2020.

Khaykin, S. M., Godin-Beekmann, S., Hauchecorne, A., Pelon, J., Ravetta, F., and Keckut, P.: Stratospheric smoke with unprecedentedly high backscatter observed by lidars above southern France, Geophys. Res. Lett., 45, https://doi.org/10.1002/2017GL076763, 2018.

Khaykin, S., Legras, B., Bucci, S., Sellitto, P., Isaksen, L., Tencé, F., Bekki, S., Bourassa, A., Rieger, L., Zawada, D., Jumelet, J., and Godin-Beekmann, S.: The 2019/20 Australian wildfires generated a persistent smoke-charged vortex rising up to 35 km altitude, Commun. Earth Environ. 1, 22 (2020). https://doi.org/10.1038/s43247-020-00022-5, 2020.

Klehr, D.: Charakterisierung der Tropopause über Ny-Alesund, Spitzbergen, Bachelor thesis, University Potsdam, http://hdl.handle.net/10013/epic.43630, 2012.

Kloss, C., Berthet, G., Sellitto, P., Ploeger, F., Taha, G., Tidiga, M., Eremenko, M., Bossolasco, A., Jégou, F., Renard, J.-B., and Legras, B.: Stratospheric aerosol layer perturbation caused by the 2019 Raikoke and Ulawun eruptions and climate impact, Atmos. Chem. Phys. Discuss., https://doi.org/10.5194/acp-2020-701, in review, 2020.

https://doi.org/10.5194/acp-2020-1271
Preprint. Discussion started: 29 December 2020

Knopf, D. A. and Alpert, P. A.: A water activity based modelof heterogeneous ice nucleation kinetics for freezing of waterand aqueous solution droplets, Farad. Discuss., 165, 513–534, doi:10.1039/c3fd00035d, 2013.

Knopf, D. A., and Rigg, Y. J., Homogeneous ice nucleation from aqueous inorganic/organic particles representative of biomass burning: Water activity, freezing temperatures, nucleation rates, J. Phys. Chem. A, 115, 762-773, https://doi.org/10.1021/jp109171g, 2011.

Knopf, D. A., Alpert, P. A., and Wang, B.:, The role of organic aerosol in atmospheric ice nucleation: a review, ACS Earth and Space Chemistry, 2, 168–202, https://doi.org/10.1021/acsearthspacechem.7b00120, 2018.

Koop, T., Luo, B. P., Tsias, A., and Peter, T.: Water activity as the determinant for homogeneous ice nucleation in aqueous solutions, Nature, 406, 611–614, doi:10.1038/35020537, 2000.

Koop, T., Bookhold, J., Shiraiwa, M., and Pöschl, U.: Glass transition and phase state of organic compounds: dependency on molecular properties and implications for secondary organic aerosols in the atmosphere, Phys. Chem. Chem. Phys., 13, 19238–19255, http://dx.doi.org/10.1039/c1cp22617g, 2011.

Korolev, A. and Leisner, T.: Review of experimental studies of secondary ice production, Atmos. Chem. Phys., 20, 11767–11797, https://doi.org/10.5194/acp-20-11767-2020, 2020.

Law, K.S. and Stohl,A.:Arctic air pollution: origins and impacts, Science, 315, 1537–1540, https://doi.org/10.1126/science.1137695, 2007.

Law, K. S., Stohl, A., Quinn, P. K., Brock, C. A., Burkhart, J. F., Paris, J.-D., Ancellet, G., Singh, H. B., Roiger, A., Schlager, H., Dibb, J., Jacob, D. J., Arnold, S. R., Pelon, J., and Thomas, J. L.: Arctic Air Pollution: New Insights from POLARCAT-IPY, Bull. Amer. Meteor. Soc., 95, 1873–1895, https://doi.org/10.1175/BAMS-D-13-00017.1, 2014.

Lawrence, Z. D., Perlwitz, J., Butler, A. H., Manney, G. L., Newman, P. A., Lee, S. H., and Nash, E. R.: The Remarkably Strong Arctic Stratospheric Polar Vortex of Winter 2020: Links to Record-Breaking Arctic Oscillation and Ozone Loss. J. Geophys. Res - Atmospheres, 125, e2020JD033271, https://doi.org/10.1029/2020JD033271, 2020.

Loewe, K., Ekman, A. M. L., Paukert, M., Sedlar, J., Tjernström, M., and Hoose, C.: Modelling micro- and macrophysical contributors to the dissipation of an Arctic mixed-phase cloud during the Arctic Summer Cloud Ocean Study (ASCOS), Atmos.Chem. Phys., 17, 6693–6704, https://doi.org/10.5194/acp-17-6693-2017, 2017

Mamouri, R.-E. and Ansmann, A.: Potential of polarization lidar to provide profiles of CCN- and INP-relevant aerosol parameters, Atmos. Chem. Phys., 16, 5905-5931, doi:10.5194/acp-16-5905-2016, 2016.

Mamouri, R.-E. and Ansmann, A.: Potential of polarization/Raman lidar to separate fine dust, coarse dust, maritime, and anthropogenicaerosol profiles, Atmos. Meas. Tech., 10, 3403-3427, https://doi.org/10.5194/amt-10-3403-2017, 2017

Manney, G. L., Livesey, N. J., Santee, M. L., Froidevaux, L., Lambert, A., Lawrence, Z. D., Millán, L. F., Neu, J. L., Read, W. G., Schwartz, M. J., and Fuller, R. A.: Record-low Arctic stratospheric ozone in 2020: MLS observations of chemical processes and comparisons with previous extreme winters. Geophys. Res. Lett., 47, e2020GL089063, https://doi.org/10.1029/2020GL089063, 2020.

Mattis, I., Seifert, P., Müller, D., Tesche, M., Hiebsch, A., Kanitz, T., Schmidt, J., Finger, F., Wandinger, U., and Ansmann, A.: Volcanic aerosol layers observed with multiwavelength Raman lidar over central Europe in 2008-–2009, J. Geophys. Res., 115, D00L04, doi:10.1029/2009JD013472, 2010.

McCluskey, C. S., Ovadnevaite, J., Rinaldi, M., Atkinson, J., Belosi, F., Ceburnis, D., Marullo, S., Hill, T. C. J., Lohmann, U., Kanji, Z. A., O'Dowd, C., Kreidenweis, S. M., and DeMott, P. J.: Marine and terrestrial organic ice-nucleating particles in pristine marine to continentally influenced Northeast Atlantic air masses, J. Geophys. Res.-Atmosphere, 123, 6196–6212, https://doi.org/10.1029/2017JD028033, 2018.

https://doi.org/10.5194/acp-2020-1271
Preprint. Discussion started: 29 December 2020

Atmospheric Chemistry and Physics Discussions

Mikhailov, E., Vlasenko, S., Martin, S. T., Koop, T., and Pöschl, U.: Amorphous and crystalline aerosol particles interacting with water vapor: conceptual framework and experimental evidence for restructuring, phase transitions and kinetic limitations, Atmos. Chem. Phys., 9, 9491–9522, https://doi.org/10.5194/acp-9-9491-2009, 2009.

Mitchell, D. L., Garnier, A., Pelon, J., and Erfani, E.: CALIPSO (IIR–CALIOP) retrievals of cirrus cloud ice-particle concentrations, Atmos. Chem. Phys., 18, 17325–17354, https://doi.org/10.5194/acp-18-17325-2018, 2018.

Morrison, H., De Boer, G., Feingold, G., Harrington, J., Shupe,M. D., and Sulia, K.: Resilience of persistent Arctic mixed-phase clouds, Nat. Geosci., 5, 11–17, 2012.

MOSAiC: MOSAiC hompegage, available at https://mosaic-expedition.org/, last access: 20 October, 2020.

Müller, D., Wandinger, U., and Ansmann, A.: Microphysical particle parameters from extinction and backscatter lidar data by inversion with regularization: Theory, Appl. Opt., 38, 2346–2357, 1999.

Müller, D., Mattis, I., Wandinger, U., Ansmann, A., Althausen, A., and Stohl, A.: Raman lidar observations of aged Siberian and Canadian forest fire smoke in the free troposphere over Germany in 2003: Microphysical particle characterization, J. Geophys. Res., 110, D17201, doi:10.1029/2004JD005756, 2005.

Müller, D., Ansmann, A., Mattis, I., Tesche, M., Wandinger, U., Althausen, D., and Pisani, G.: Aerosol-type-dependent lidar ratios observed with Raman lidar, J. Geophys. Res., 112, D16202, doi:10.1029/2006JD008292, 2007.

Müller, D., Hostetler, C. A., Ferrare, R. A., Burton, S. P., Chemyakin, E., Kolgotin, A., Hair, J. W., Cook, A. L., Harper, D. B., Rogers, R. R., Hare, R. W., Cleckner, C. S., Obland, M. D., Tomlinson, J., Berg, L. K., and Schmid, B.: Airborne Multiwavelength High Spectral Resolution Lidar (HSRL-2) observations during TCAP 2012: vertical profiles of optical and microphysical properties of a smoke/urban haze plume over the northeastern coast of the US, Atmos. Meas. Tech., 7, 3487–3496, https://doi.org/10.5194/amt-7-3487-2014, 2014

Murray, B. J., Wilson, T. W., Dobbie, S., Cui, Z., Al-Jumur, S. M. R. K., Möhler, O., Schnaiter, M., Wagner, R., Benz, S., Niemand, M., Saathoff, H., Ebert, V., Wagner, S., and Kärcher, B.: Heterogeneous nucleation of ice particles on glassy aerosols under cirrus conditions, Nature Geoscience, 3, 233-237, doi:10.1038/ngeo817, 2010.

Noel, V. and Sassen, K.: Study of planar ice crystal orientations in ice clouds from scanning polarization lidar observations, J. Appl.Meteorol., 44, 653-664, 2005.

Noel, V. and Chepfer, H.: A global view of horizontally oriented crystals in ice clouds from Cloud-Aerosol Lidar and Infrared Pathfinder Satellite Observation (CALIPSO), J. Geophys. Res., 115, D00H23, https://doi.org/10.1029/2009JD012365, 2010.

Nott, G.J. and Duck, T.J.: Lidar studies of the polar troposphere. Met. Apps, 18, 383-405. doi:10.1002/met.289, 2011.

Ohneiser, K., Ansmann, A., Baars, H., Seifert, P., Barja, B., Jimenez, C., Radenz, M., Teisseire, A., Floutsi, A., Haarig, M., Foth, A., Chudnovsky, A., Engelmann, R., Zamorano, F., Bühl, J., and Wandinger, U.: Smoke of extreme Australian bushfires observed in the stratosphere over Punta Arenas, Chile, in January 2020: optical thickness, lidar ratios, and depolarization ratio sat 355 and 532 nm,, Atmos. Chem. Phys., 20, 8003-8015, https://doi.org/10.5194/acp-20-8003-2020, 2020.

Ohneiser, K., Ansmann, A., Engelmann, R., Griesche, H., Radenz, M., Hofer, J., Althausen, D., Baars, H., Ritter, C., and Veselovskii, I.: The UTLS wildfire smoke layer over the North Pole in the winter half year of 2019-2020: vertical structures, optical and microphysical properties, and decay behavior, in preparation for Atmos. Chem. Phys., 2021.

Pappalardo, G., Amodeo, A., Apituley, A., Comeron, A., Freudenthaler, V., Linné, H., Ansmann, A., Bösenberg, J., D'Amico, G., Mattis, I., Mona, L., Wandinger, U., Amiridis, V., Alados-Arboledas, L., Nicolae, D., and Wiegner, M.: EARLINET: towards an advanced sustainable European aerosol lidar network, Atmos. Meas. Tech., 7, 2389–2409, doi:10.5194/amt-7-2389-2014, 2014.

https://doi.org/10.5194/acp-2020-1271
Preprint. Discussion started: 29 December 2020

Paukert, M. and Hoose, C.: Modeling immersion freezing with aerosol-dependent prognostic ice nuclei in Arctic mixed-phaseclouds, J. Geophys. Res.-Atmos., 119, 9073–9092, 2014

Peterson, D. A., Campbell, J. R., Hyer, E. J., Fromm, M. D., Kablick III, G. P., Cossuth, J. H., and DeLand, M. T.: Wildfire-driven thunderstorms cause a volcano-like stratospheric injection of smoke, npj Climate and Atmospheric Science, 1, article number 30, https://doi.org/10.1038/s41612-018-0039-3, 2018.

Petzold, A., Weinzierl, B., Huntrieser, H., Stohl, A., Real, E., Cozic, J., Fiebig, M., Hendricks, J., Lauer, A., Law, K., Roiger, A., Schlager, H., and Weingartner, E.: Perturbation of the European free troposphere aerosol by North American forest fire plumes during the ICARTT-ITOP experiment in summer 2004, Atmos. Chem. Phys., 7, 5105-5127, doi:10.5194/acp-7-5105-2007, 2007.

Polarstern: Alfred-Wegener-Institut Helmholtz-Zentrum für Polar- und Meeresforschung, Polar Research and Supply Vessel POLARSTERN Operated by the Alfred-Wegener-Institute, Journal of large-scale research facilities, 3, A119, http://dx.doi.org/10.17815/jlsrf-3-163, 2017.

PollyNet: PollyNET lidar data base, available at: http://polly.rsd.tropos.de/, last access: 20 October 2020.

Quennehen, B., Schwarzenboeck, A., Matsuki, A., Burkhart, J. F., Stohl, A., Ancellet, G., and Law, K. S.: Anthropogenic and forest fire pollution aerosol transported to the Arctic: observations from the POLARCAT-France spring campaign, Atmos. Chem. Phys., 12, 6437–6454, https://doi.org/10.5194/acp-12-6437-2012, 2012.

Rigg, Y. J., Alpert, P. A., and Knopf, D. A.: Immersion freezing of water and aqueous ammonium sulfate droplets initiated by humic-like substances as a function of water activity, Atmos. Chem. Phys., 13, 6603–6622, https://doi.org/10.5194/acp-13-6603-2013, 2013.

Rolph, G., Stein, A., and Stunder, B.: Real-time Environmental Applications and Display sYstem: READY. Environmental Modelling & Software, 95, 210-228, https://doi.org/10.1016/j.envsoft.2017.06.025, 2017.

Schill, G. P., DeMott, P. J., Emerson, E. W., Rauker, A. M. C., Kodros, J. K., Suski, K. J., Hill, T. C. J., Levin, E. J. T., Pierce, J. R., Farmer, D. K., and Kreidenweis, S. M.: The contribution of black carbon to global ice nucleating particle concentrations relevant to mixed-phase clouds, Proceedings of the National Academy of Sciences, 117, 22705-22711, doi: 10.1073/pnas.2001674117, 2020.

Stein, A.F., Draxler, R.R, Rolph, G.D., Stunder, B.J.B., Cohen, M.D., and Ngan, F.: NOAA's HYSPLIT atmospheric transport and dispersion modeling system, Bull. Amer. Meteor. Soc., 96, 2059-2077, http://dx.doi.org/10.1175/BAMS-D-14-00110.1, 2015

Sakai, T., Uchino, O., Nagai, T., Liley, B., Morino, I., and Fujimoto, T.: Long-term variation of stratospheric aerosols observed with lidars over Tsukuba, Japan, from 1982 and Lauder, New Zealand, from 1992 to 2015, J. Geophys. Res. Atmos., 121, 10283-10293, doi:10.1002/2016JD025132, 2016.

Slade, J. H., Shiraiwa, M., Arangio, A., Su, H., Pöschl, U., Wang, J., and Knopf, D. A.: Cloud droplet activation through oxidation of organic aerosol influenced by temperature and particle phase state, Geophys. Res. Lett., 44, 1583– 1591, doi:10.1002/2016GL072424, 2017.

Stohl,A.: Characteristics of atmospheric transport into the Arctic troposphere, J. Geophys. Res., 111, D11306, https://doi.org/10.1029/2005JD006888, 2006.

Torres, O., Bhartia, P. K., Taha, G., Jethva, H., Das, S., Colarco, P., Krotkov, N., Omar, A., and Ahn, C.: Stratospheric Injection of Massive Smoke Plume from Canadian Boreal Fires in 2017 as seen by DSCOVR-EPIC, CALIOP and OMPS-LP Observations. Journal of Geophysical Research: Atmospheres, 125, e2020JD032579, https://doi.org/10.1029/2020JD032579, 2020.

Vaughan, G., Wareing, D., and Ricketts, H.: Measurement Report: Lidar measurements of stratospheric aerosol following the Raikoke and Ulawun volcanic eruptions, Atmos. Chem. Phys. Discuss., https://doi.org/10.5194/acp-2020-982, in review, 2020.

Verlinde, J., Harrington, J. Y., McFarquhar, G. M., Yannuzzi, V. T.,Avramov, A., Greenberg, S., Johnson, N., Zhang, G., Poellot, M.R., Mather, J. H., Turner, D. D., Eloranta, E. W., Zak, B. D.,Prenni, A. J., Daniel, J. S., Kok, G. L., Tobin, D. C., Holz, R.,Sassen, K.,

https://doi.org/10.5194/acp-2020-1271
Preprint. Discussion started: 29 December 2020

Spangenberg, D., Minnis, P., Tooman, T. P., Ivey, M.D., Richardson, S. J., Bahrmann, C. P., Shupe, M., DeMott, P.J., Heymsfield, A. J., and Schofield, R.: The mixed-phase Arctic cloud experiment, B. Am. Meteorol. Soc., 88, 205–221, 2007

Veselovskii I., Kolgotin, A., Griaznov, V., Müller, D., Wandinger, U., and Whiteman, D.: Inversion with regularization for the retrieval of tropospheric aerosol parameters from multi-wavelength lidar sounding, Appl. Opt., 41, 3685–3699, https://doi.org/10.1364/AO.41.003685, 2002.

Veselovskii, I., Dubovik, O., Kolgotin, A., Korenskiy, M., Whiteman, D. N., Allakhverdiev, K., and Huseyinoglu, F.: Linear estimation of particle bulk parameters from multi-wavelength lidar measurements, Atmos. Meas. Tech., 5, 1135–1145, doi:10.5194/amt-5-1135-2012, 2012.

Vihtakari, M: ggOceanMaps: Plot data on oceanographic maps using 'ggplot2', 2020, https://mikkovihtakari.github.io/ggOceanMaps, https://github.com/MikkoVihtakari/ggOceanMaps.

Wandinger, U., Ansmann, A., Reichardt, J., and Deshler, T.: Determination of stratospheric aerosol microphysical properties from independent extinction and backscattering measurements with a Raman lidar, Appl. Opt., 34, 8315–8329, https://doi.org/10.1364/AO.34.0083151995, 1995.

Wang, Q., Jacob, D. J., Fisher, J. A., Mao, J., Leibensperger, E. M., Carouge, C. C., Le Sager, P., Kondo, Y., Jimenez, J. L., Cubison, M. J., and Doherty, S. J.: Sources of carbonaceous aerosols and deposited black carbon in the Arctic in winter-spring: implications for radiative forcing, Atmos. Chem. Phys., 11, 12453–12473, https://doi.org/10.5194/acp-11-12453-2011, 2011.

Wang, B., and Knopf, D. A.: Heterogeneous ice nucleation on particles composed of humic-like substances impacted by O_3, J. Geophys. Res., 116, D03205, doi:10.1029/2010JD014964, 2011.

Wang, B., Lambe, A. T., Massoli, P., Onasch, T. B., Davidovits, P., Worsnop, D. R., and Knopf, D. A.: The deposition ice nucleation and immersion freezing potential of amorphous secondary organic aerosol: Pathways for ice and mixed-phase cloud formation, J. Geophys. Res., 117, D16209, doi:10.1029/2012JD018063, 2012.

Wendisch, M., Macke, A., Ehrlich, A., Lüpkes, C., Mech, M.,Chechin, D., Dethloff, K., Velasco, C. B., Bozem, H., Brückner, M., Clemen, H.-C., Crewell, S., Donth, T., Dupuy, R., Ebell, K., Egerer, U., Engelmann, R., Engler, C., Eppers, O., Gehrmann,M., Gong, X., Gottschalk, M., Gourbeyre, C., Griesche, H., Hartmann, J., Hartmann, M., Heinold, B., Herber, A., Herrmann, H.,Heygster, G., Hoor, P., Jafariserajehlou, S., Jäkel, E., Järvinen, E.,Jourdan, O., Kästner, U., Kecorius, S., Knudsen, E. M., Köllner, F., Kretzschmar, J., Lelli, L., Leroy, D., Maturilli, M., Mei, L., Mertes, S., Mioche, G., Neuber, R., Nicolaus, M., Nomokonova,T., Notholt, J., Palm, M., van Pinxteren, M., Quaas, J., Richter,P., Ruiz-Donoso, E., Schäfer, M., Schmieder, K., Schnaiter, M., Schneider, J., Schwarzenböck, A., Seifert, P., Shupe, M. D., Siebert, H., Spreen, G., Stapf, J., Stratmann, F., Vogl, T., Welti,A., Wex, H., Wiedensohler, A., Zanatta, M., and Zeppenfeld, S.: The Arctic cloud puzzle: using ACLOUD/PASCAL multiplatform observations to unravel the role of clouds and aerosol particles in Arctic amplification, Bull. Am. Meteorol. Soc., 100, 841–871, https://doi.org/10.1175/BAMS-D-18-0072.1, 2019.

Willis, M. D., Leaitch, W. R., and Abbatt, J. P.: Processes controlling the composition and abundance of Arctic aerosol. Reviews of Geophysics, 56, 621-671, https://doi.org/10.1029/2018RG000602, 2018.

Willis, M. D., Bozem, H., Kunkel, D., Lee, A. K. Y., Schulz, H., Burkart, J., Aliabadi, A. A., Herber, A. B., Leaitch, W. R., and Abbatt, J. P. D.: Aircraft-based measurements of High Arctic springtime aerosol show evidence for vertically varying sources, transport and composition, Atmos. Chem. Phys., 19, 57–76, https://doi.org/10.5194/acp-19-57-2019, 2019.

WMO: World Meteorological Organisation, International Meterological Vocabulary, No. 182, ISBN 92-63-02182-1, 1992.

https://doi.org/10.5194/acp-2020-1271
Preprint. Discussion started: 29 December 2020

Wohltmann, I., von der Gathen, P., Lehmann, R., Maturilli, M., Deckelmann, H., Manney, G. L., Davies, J., Tarasick, D., Jepsen, N., Kivi, R., Lyall, N., and Rex, M.: Near-complete local reduction of Arctic stratospheric ozone by severe chemical loss in spring 2020. Geophysical Research Letters, 47, e2020GL089547, https://doi.org/10.1029/2020GL089547, 2020.

Yang, Y., Zhao, C., Wang, Q., Cong, Z., Yang, X., and Fan, H.: Aerosol Characteristics in the Three Poles of the Earth Observed by CALIPSO, Atmos. Chem. Phys. Discuss., https://doi.org/10.5194/acp-2020-1159, in review, 2020.

Yin, Z., Ansmann, A., Baars, H., Seifert, P., Engelmann, R., Radenz, M., Jimenez, C., Herzog, A., Ohneiser, K., Hanbuch, K., Blarel, L., Goloub, P., Dubois, G., Victori, S., and Maupin, F.: Aerosol measurements with a shipborne Sun–sky–lunar photometer and collocated multiwavelength Raman polarization lidar over the Atlantic Ocean, Atmos. Meas. Tech., 12, 5685–5698, https://doi.org/10.5194/amt-12-5685-2019, 2019.

Yu, P., Toon, O. B., Bardeen, C. G., Zhu, Y., Rosenlof, K. H., Portmann, R. W., Thornberry, T. D., Gao, R.-S., Davis, S. M., Wolf, E. T., de Gouw, J., Peterson, D. A., Fromm, M. D., and Robock, A.: Black carbon lofts wildfire smoke high into the stratosphere to form a persistent plume, Science, 365, 587–590, doi: 10.1126/science.aax1748, 2019.

Zuev, V. V., Gerasimov, V. V., Nevzorov, A. V., and Savelieva, E. S.: Lidar observations of pyrocumulonimbus smoke plumes in the UTLS over Tomsk (Western Siberia, Russia) from 2000 to 2017, Atmos. Chem. Phys., 19, 3341–3356, https://doi.org/10.5194/acp-19-3341-2019, 2019.

https://doi.org/10.5194/acp-2020-1271
Preprint. Discussion started: 29 December 2020

Atmospheric Chemistry and Physics Discussions

Table 1. Overview of Polly observational products. r denotes aerosol particle radius.

Aerosol/cloud optical properties	Wavelength
Backscatter coefficient [Mm^{-1} sr^{-1}]	355, 532, 1064 nm
Extinction coefficient [Mm^{-1}]	355, 532 nm
Lidar ratio [sr]	355, 532 nm
Depolarization ratio	355, 532 nm
Aerosol microphysical properties	
Volume size distribution [μm^3 m^{-3} μm^{-1}]	
Volume concentration [μm^3 m^{-3}]	
Mass concentration [μg m^{-3}]	
Surface-area concentration [cm^2 m^{-3}]	
Number concentration (r >50 nm) [cm^{-3}]	
Number concentration (r >250 nm) [cm^{-3}]	
CCN concentration [cm^{-3}]	
INP concentration [L^{-1}]	
Droplet microphysical properties (liquid water clouds)	
Droplet number concentration [cm^{-3}]	
Droplet effective radius [μm]	
Liquid water content [g m^{-3}]	
Water vapor fields	
Water-vapor-to-dry-air mixing ratio [g kg^{-3}]	
Relative humidity [%]	

https://doi.org/10.5194/acp-2020-1271
Preprint. Discussion started: 29 December 2020

Atmospheric Chemistry and Physics Discussions

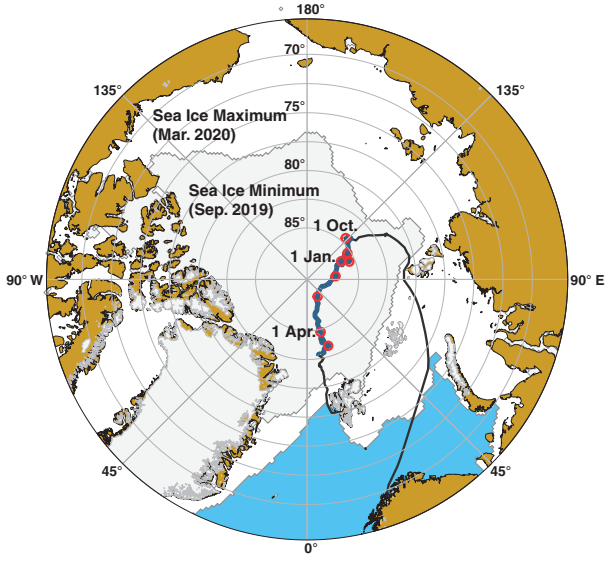

Figure 1. Travel (black) and drifting (blue) route of RV Polarstern from 1 October 2019 to 1 May 2020. Each of the eight red circles marks the beginning of the next month. The map was produced with 'ggOceanMaps' (Vihtakari, 2020) by using Sea Ice Index Version 3 data (Fetterer et al., 2020).

Figure 2. Polarstern drifting in the Arctic ice on 10 April 2020 (left panel) and measurement containers for in situ aerosol monitoring (the two first containers on the left side and the first container on the right side), and for remote sensing of aerosols and clouds (right panel). The OCEANET container of TROPOS is the third one on the left side. The ARM mobile facility (AMT-1) is shown on the right side. The photographs are taken by Michael Gutsche (CC-BY 4.0), AWI.

https://doi.org/10.5194/acp-2020-1271
Preprint. Discussion started: 29 December 2020

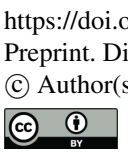

Atmospheric Chemistry and Physics Discussions

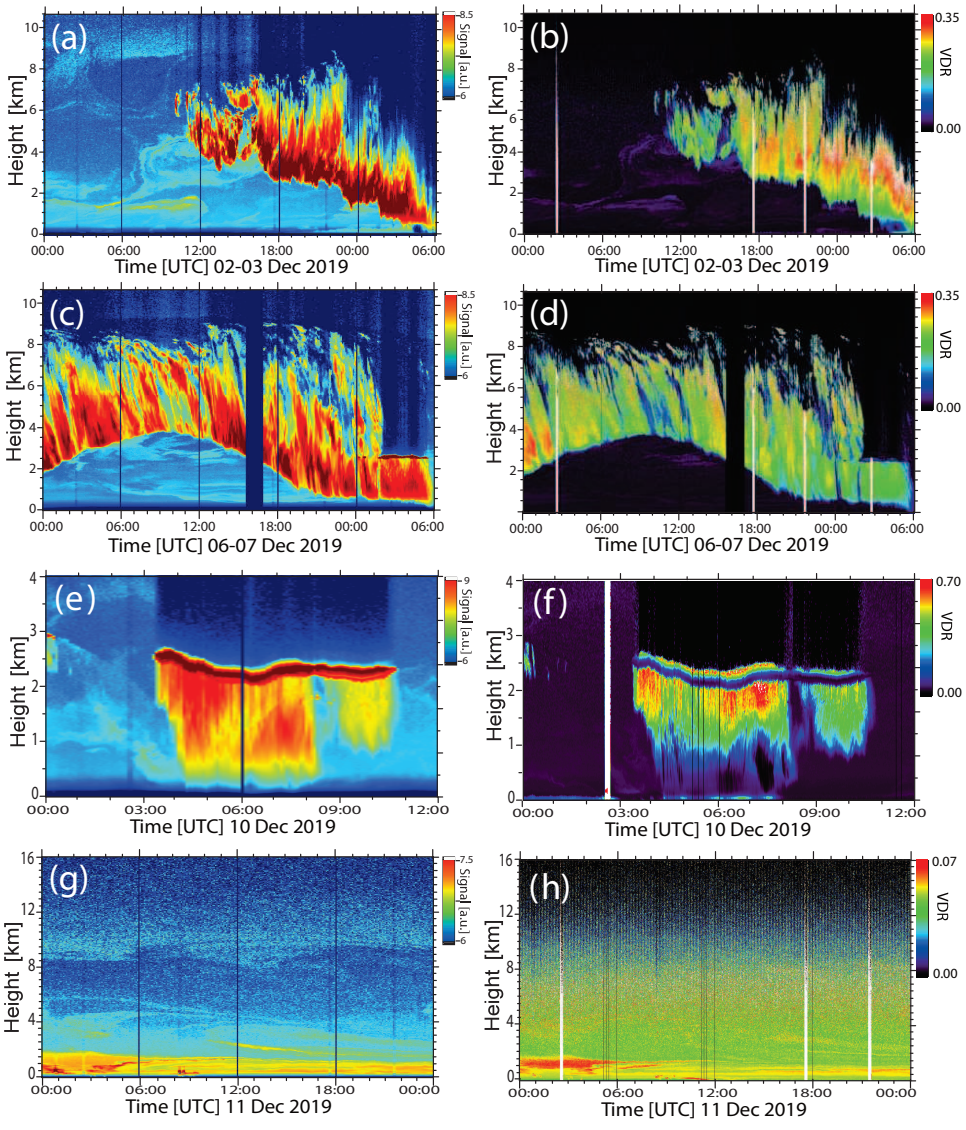

Figure 3. Ice clouds, mixed-phase clouds, and aerosols monitored with Polly aboard RV Polarstern from 2–12 December 2019. (a-d) Evolution of cirrus layers with strong virga embedded in wildfire smoke and Arctic haze, (e-f) development of a long-lasting mixed-phase altocumulus with shallow liquid-water layer at the top and ice virga below, and (g-h) Arctic haze (below 5 km height) and wildfire smoke (above 8 km) during clear sky conditions. The range-corrected 1064 nm signal (left panels, in arbitrary units, a. u.) and the 532 nm volume depolarization ratio (VDR, right panels) are shown.

https://doi.org/10.5194/acp-2020-1271
Preprint. Discussion started: 29 December 2020

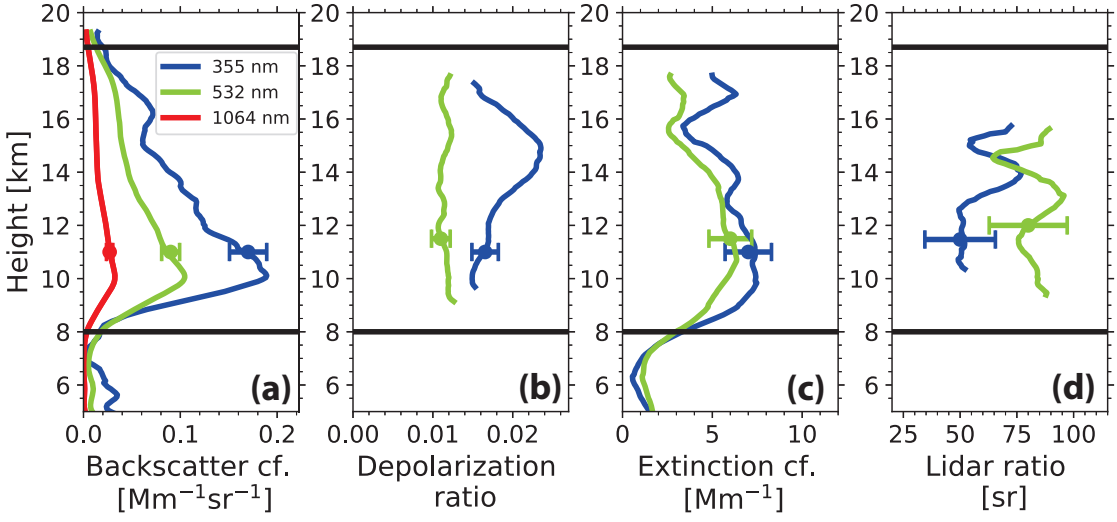

Figure 4. Profiles of optical properties (24 h mean values) of the wildfire smoke layer on 11 December 2019. Base and top heights of the smoke layer are indicated by black horizontal lines. (a) Particle backscatter coefficient at three wavelengths, (b) particle linear depolarization ratio at 355 and 532 nm, (c) smoke extinction coefficient at 355 and 532 nm, and d) respective smoke extinction-to-backscatter ratio (lidar ratio) are shown. All basic lidar signal profiles were strongly smoothed with vertical window lengths of 2000 m to strongly reduce the signal noise. Error bars indicate the estimated uncertainties.

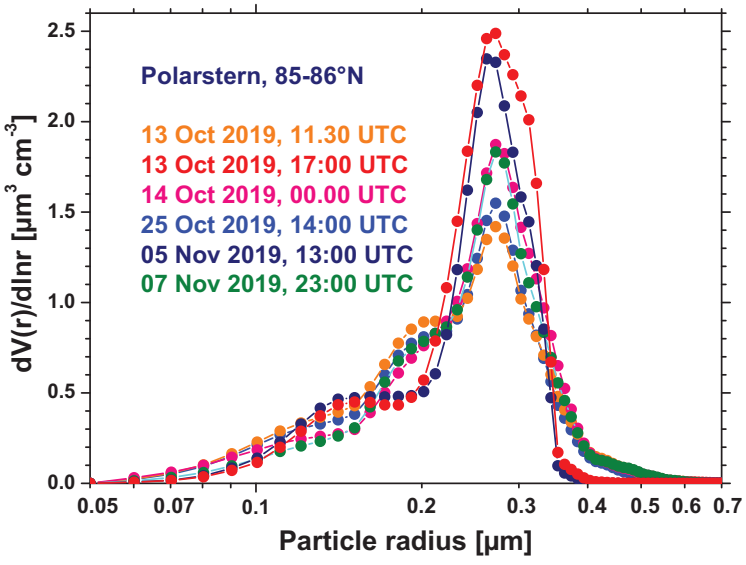

Figure 5. Size distributions of the stratospheric smoke particles retrieved from the multiwavelength lidar observations on five days in October and November 2019. A narrow accumulation mode with particle sizes (diameters) from 400 to 1000 nm and a weak Aitken mode to the left is typical for aged wildfire smoke particles.

https://doi.org/10.5194/acp-2020-1271
Preprint. Discussion started: 29 December 2020

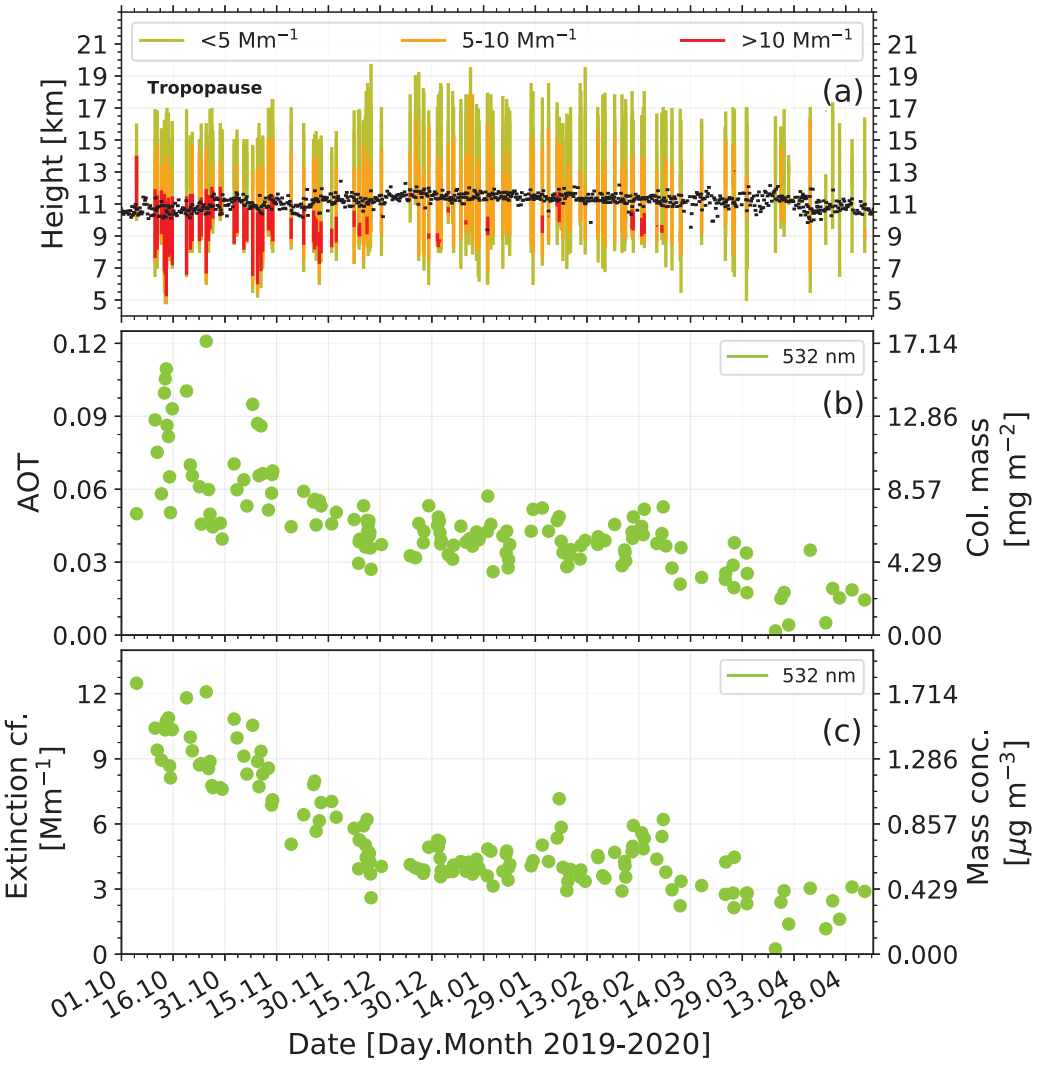

Figure 6. (a) Overview of Polly observations of the UTLS smoke layer (colored bars from bottom to top, one bar per day) for the winter half year (October 2019 to April 2020). Observational gaps between bars are caused by opaque low level clouds and fog. The color in the bars provides information about the smoke particle concentration in terms of particle extinction coefficient at 532 nm. The tropopause separates the tropospheric from the stratospheric part of the smoke layer. (b) 532 nm AOT of the smoke layer and respective column mass concentration. (c) Smoke layer mean 532 nm particle extinction coefficient and corresponding vertical mean particle mass concentration. For comparison, background extinction coefficients are expected to be of the order of 0.1–0.2 Mm^{-1} as observed over northern midlatitudes (Baars et al., 2019).

https://doi.org/10.5194/acp-2020-1271
Preprint. Discussion started: 29 December 2020

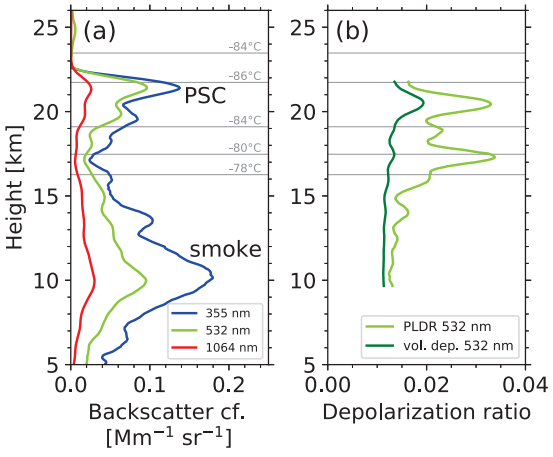

Figure 7. Polar stratospheric cloud (PSC) from 17.5–22.5 km height on top of the smoke layer on 14 January 2020, 21-24 UTC. Particle backscatter coefficients and volume and particle linear depolarization ratio (PLDR) are shown. The optical properties values are indicative for PSC Ib type. The 532 nm backscatter ratio (total-to-Rayleigh backscatter) peaks at 2.43. PSC optical thickness was 0.0125 at 532 nm (computed from backscatter values multiplied by a lidar ratio of 50 sr). Horizontal gray lines show different temperature levels.

https://doi.org/10.5194/acp-2020-1271
Preprint. Discussion started: 29 December 2020

Atmospheric Chemistry and Physics Discussions

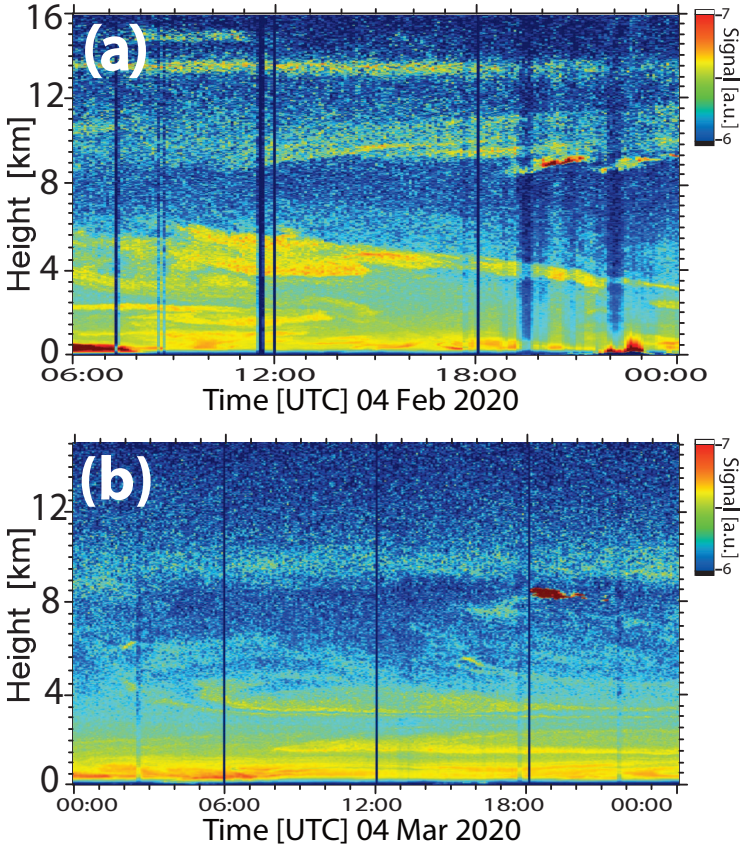

Figure 8. Artic haze (below 8 km height) and wildfire smoke (above 8 km height) over the North Pole region in late winter on (a) 4 February 2020 and (b) 4 March 2020. PSC layers are present as well at 13.5 and 15 km height on 4 February (pronounced yellow layers). The range-corrected 1064 nm signal is shown in arbitray units (a.u.).

https://doi.org/10.5194/acp-2020-1271
Preprint. Discussion started: 29 December 2020

Atmospheric Chemistry and Physics Discussions

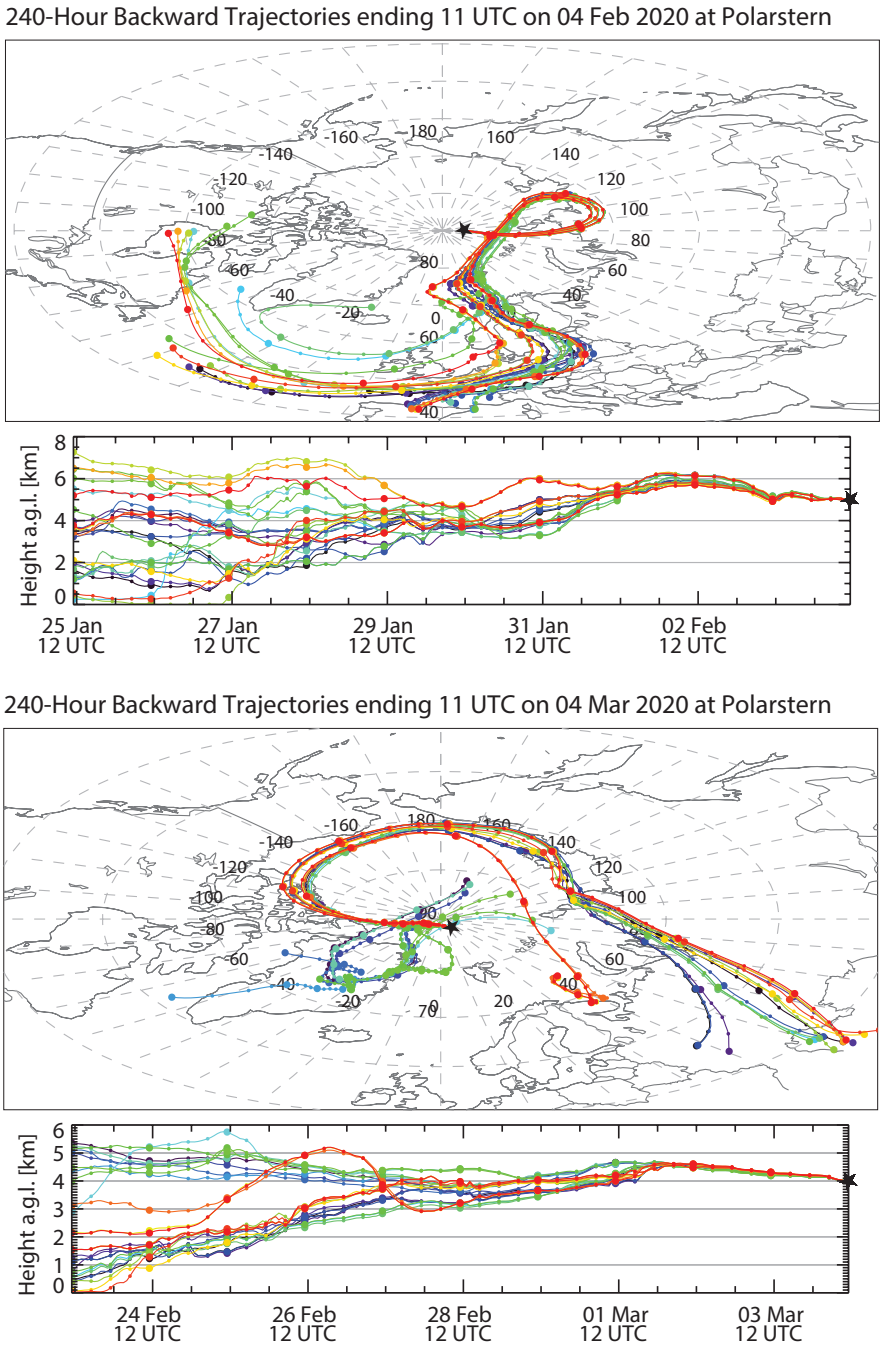

Figure 9. (a) 10-day ensemble backward trajectories for (a) 4 February 2020, 11 UTC arrival time, and 5km arrival height and (b) 4 March 2020, 11 UTC arrival time, and 4 km arrival height (HYSPLIT, 2020; Stein et al., 2015; Rolph et al., 2017).

https://doi.org/10.5194/acp-2020-1271
Preprint. Discussion started: 29 December 2020

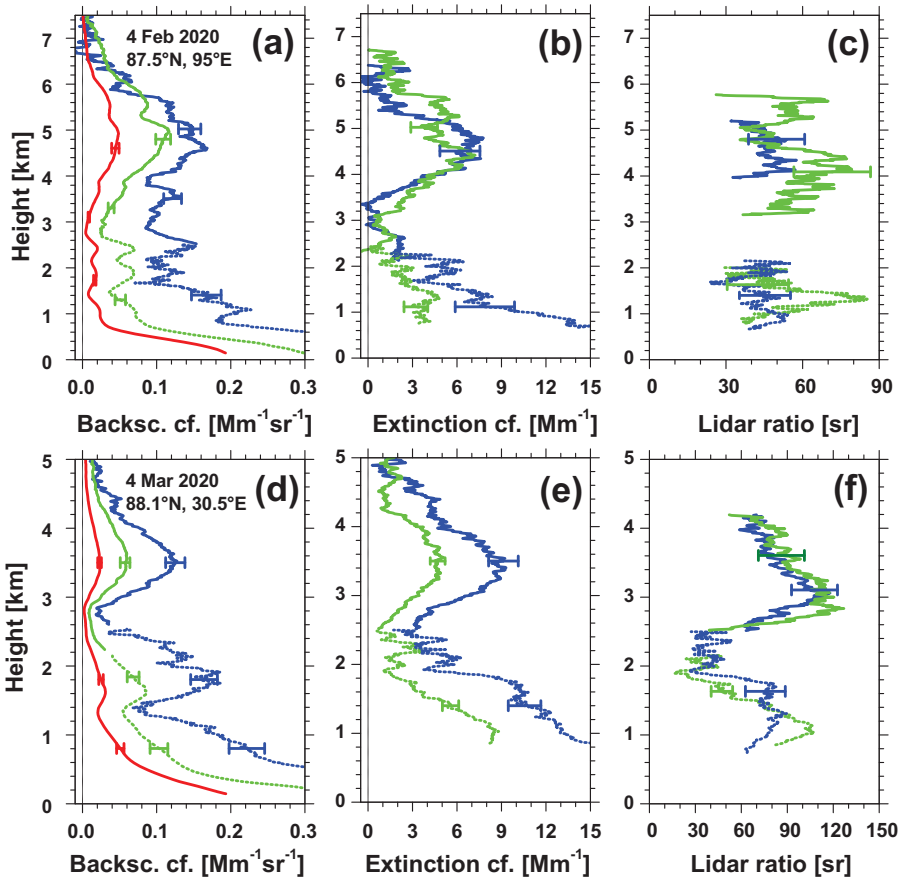

Figure 10. Artic haze backscatter, extinction, and extinction-to-backscatter ratios (lidar ratios). Mean profiles for 4 February 2020, 6:00–17:37 UTC, and for 4 March 2020, 0:00–17:45 UTC, are shown. A composite of near-range and far-range lidar observations (near range data up to 2-3 km height) is presented. Lidar signals are smoothed with vertical window lenghts of 300 m (backscatter) and 900 m (extinction, lidar ratio). Error bars indicate the uncertainty in the computations. 532 nm AOT was 0.024 on 4 February (for heights up to 7 km) and 0.022 on 4 March (for heights up to 5 km).

https://doi.org/10.5194/acp-2020-1271
Preprint. Discussion started: 29 December 2020

Atmospheric Chemistry and Physics Discussions

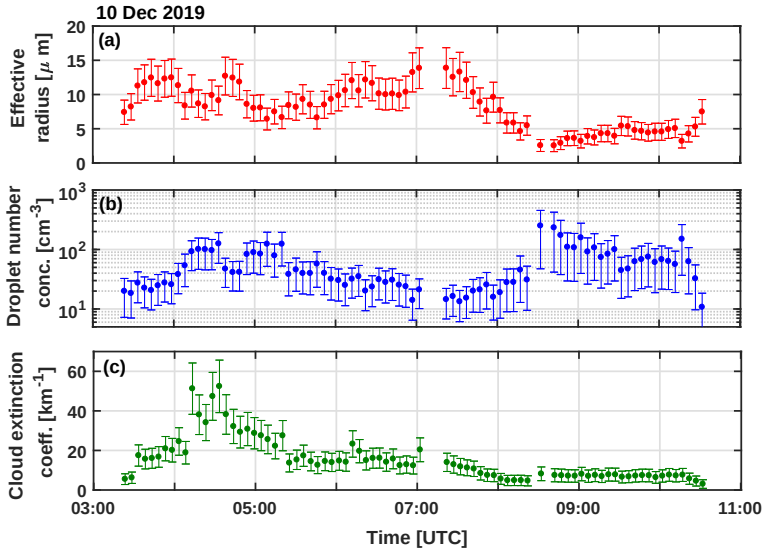

Figure 11. (a) Effective radius of cloud droplets, (b) cloud droplet number concentration, and (c) cloud extinction coefficient for the altocumulus layer in Fig. 3e. The effective radius can be interpreted as the characteristic droplet radius. All parameters are retrieved for the height of 75 m above cloud base. Error bars indicate the uncertainty range.

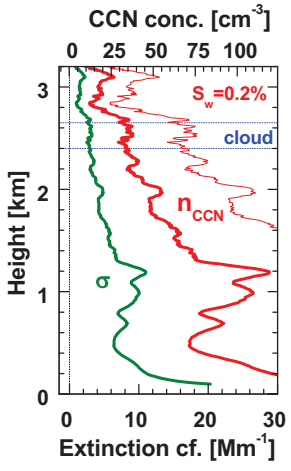

Figure 12. Aerosol observation on 10 Dec 2019, 2:15-2:45 UTC, just before the altocumulus layer was detected over the lidar station (see Fig. 3e). The height profile of the extinction coefficient σ is estimated from the backscatter coefficient profile (assuming a lidar ratio fo 30 sr as indicated by our Raman lidar observation) and then converted into cloud condensation nucleus concentrations (n_{CCN}, for a water supersaturation of 0.2%) by assuming (fresh) central European anthropogenic haze (thin solid red, large fraction of small particles serving as CCN) and aged long-transported haze (thick solid red, low fraction of favorable small CCN) with a 50% smaller CCNC. Cloud base and top heights of the altocumulus layer at 3:00 UTC are indicated by horizontal lines.

https://doi.org/10.5194/acp-2020-1271
Preprint. Discussion started: 29 December 2020

Atmospheric Chemistry and Physics Discussions

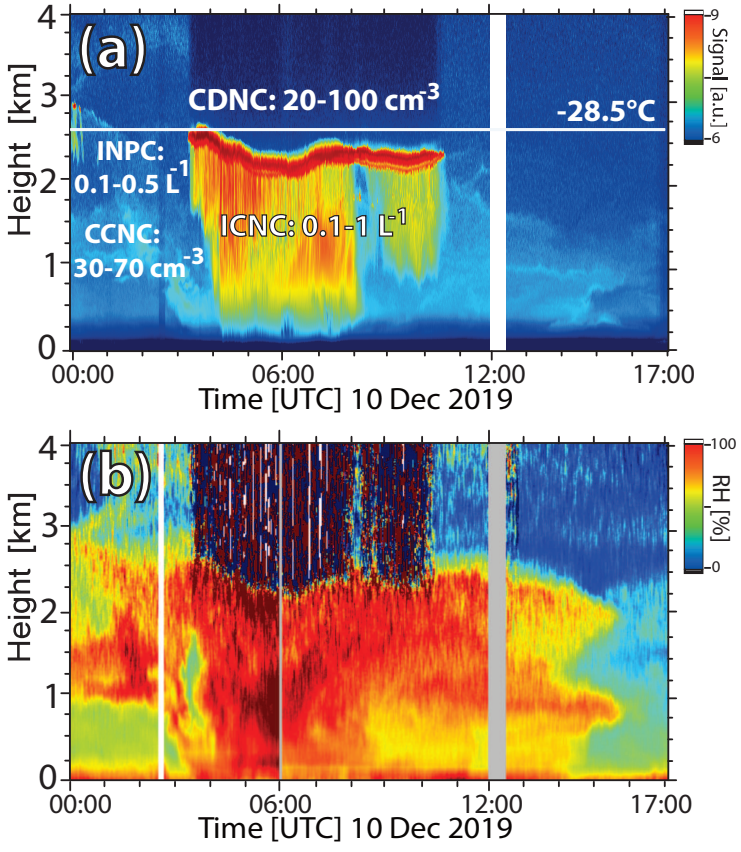

Figure 13. (a) Successful mixed-phase-cloud closure experiment indicated by the good match between cloud condensation nucleus concentration (CCNC) and cloud droplet number concentration (CDNC) and, on the other hand, between ice-nucleating particle concentration (INPC) and ice crystal number concentration (ICNC). All numbers are retrieved from observations between 2:00 and 5:00 UTC. (b) Relative humidity field indicating high humidity within the droplet-dominated cloud top layer and in the virga zone (before 8:00 UTC) caused by strong evaporation of ice crystals. The range-corrected 1064 nm signal in (a) is biased by an detector overload in the nearest height range to the lidar. The ice crystals reached the ground between 4:15 and 8:15 UTC.

https://doi.org/10.5194/acp-2020-1271
Preprint. Discussion started: 29 December 2020

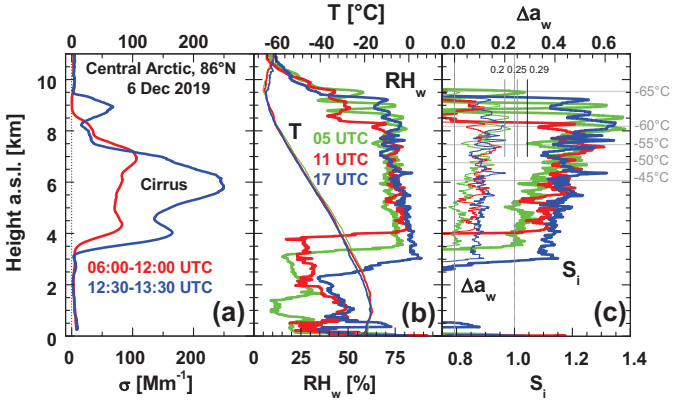

Figure 14. (a) Temporally averaged (mean) cirrus extinction coefficient σ for two observational periods from 6-12 UTC (red) and from 12:30-13:30 UTC (blue), (b) profiles of temperature T and relative humidity RH_w (over water) observed with radiosondes launched at 5, 11, and 17 UTC on 6 December 2019, and (c) water activation criterium Δa_w and ice supersaturation S_i computed from the temperature and water vapour observations shown in (b).

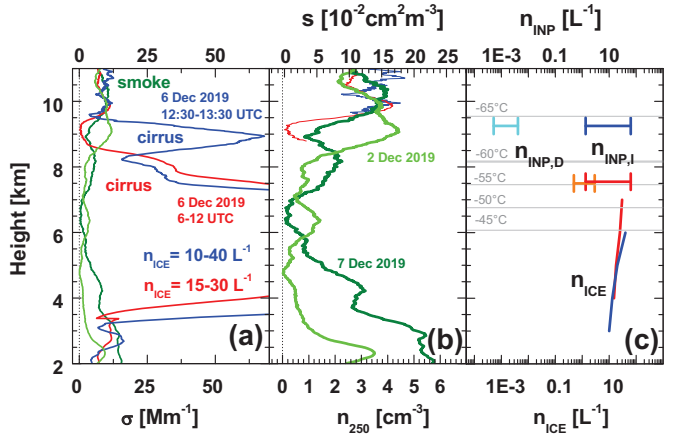

Figure 15. (a) Temporally averaged (mean) cirrus extinction coefficient σ for two observational periods from 6-12 UTC (red) and from 12:30-13:30 UTC (blue). In green and olive colors, aerosol extinction coefficient profiles at cloud free conditions on 2 and 7 December, respectively, are shown as well. Ice crystal number concentrations for the lower half of the cirrus layers are given as numbers. (b) Smoke particle number concentration n_{250} for large particles with diameters >500 nm and particle surface area concentration s derived from the lidar observations for the cloud-free days of 2 and 7 December (green, olive) and for 6 December (in red and blue, above the cirrus), and (c) derived ranges of INP number concentrations $n_{\mathrm{INP,I}}$ (for immersion freezing, blue and red, indicating the respective cirrus layers in (a)) and $n_{\mathrm{INP,D}}$ (for deposition nucleation, in orange and cyan) at the cloud top. The range of uncertainty is of the order of a factor of 2 in the case of n_{ICE}.